35

Determination of Top-of-Atmosphere Longwave Radiative Fluxes: A Comparison between two approaches using ScaRaB data

Ting Chen

Columbia University/NASA Goddard Institute for Space Studies, New York, NY 10025

William B. Rossow

NASA Goddard Institute for Space Studies, New York, NY 10025

Abstract

Two conceptually different approaches (broadband-based ERBE and narrowband-based ISCCP approaches), used to derive the TOA longwave radiative fluxes, are compared using the ScaRaB simultaneous narrowband and broadband measurements. This study directly shows that the ERBE MLE-derived cloud covers implicitly contain some information on the cloud optical properties. A spurious view-zenith-angle dependence of the MLE scene identification scheme is confirmed by this study. Except for very thin cirrus clouds, differences between the ERBE and ISCCP approaches are in general < 10 W m^{-2} for the TOA LW radiative fluxes. For clear pixels, the model calculated (ISCCP approach) TOA LW radiances are systematically smaller than the observations. Though the bias is found to be correlated on the column precipitable water amount, the exact source of this discrepancy remains undetermined and merits further study. Compared with the radiative transfer model used in this study, the ERBE LW ADMs are too weakly limb-darkened for optically thin clouds, but too strongly limb-darkened for optically thick clouds, indicating that more accurate instantaneous TOA LW flux estimations from the ERBE approach would require additional cloud classes based on cloud height and optical thickness.

1. Introduction

The delicate balance between the incoming shortwave radiation and the outgoing longwave radiation at the top of the atmosphere (TOA) and its subtle regional variations is a direct indicator of the net gain/loss of radiant energy by our planet that determines the state of the atmospheric general circulation and the climate. Accurate knowledge of these two flux components is crucial for understanding the climate system and predicting climate change due to human activities, since the atmospheric circulation is forced by the vertical and horizontal gradients (i.e., differences) in radiative and latent heating/cooling, not by their magnitude. The TOA outgoing longwave radiation (OLR) can be directly estimated from satellite measurements of broadband radiances, such as the *Nimbus-7* Earth Radiation Budget (*Nimbus-7* ERB; Jacobowitz et al. 1984), the Earth Radiation Budget Experiment (ERBE; Barkstrom and Smith 1986; Barkstrom et al. 1989), the Scanner for Radiation Budget (ScaRaB; Kandel et al. 1994), and the ongoing Clouds and the Earth's Radiant Energy System (CERES; Wielicki et al. 1996). Alternatively, OLR can also be indirectly inferred from narrowband radiances, either by a regression-based narrowband-to-broadband conversion technique (e.g., Ohring et al., 1984; Gruber and Krueger 1984) or by a detailed radiative transfer calculation with the cloud and surface radiative properties retrieved from narrowband radiances (e.g., the International Satellite Cloud Climatology Project, ISCCP; Schiffer and Rossow 1983; Rossow and Schiffer 1991) and other correlative atmospheric and surface datasets as input to the radiative transfer model (e.g., Rossow and Lacis 1990; Zhang et al. 1995; Rossow and Zhang 1995; Hatzianastassiou and Vardavas 1999; Chen et al. 2000a,b). The narrowband-to-broadband conversion technique is still used in some operational earth radiation budget (ERB) products at present (e.g., Gruber and Krueger 1984) despite the limitations in the single-channel narrowband to broadband algorithm (Gruber et al. 1994). With the advent of more accurate global observations of cloud, atmosphere and surface properties from satellites, the approach which calculates broadband fluxes from retrieved physical quantities becomes more attractive since it intrinsically separates the effects of the clouds on the radiation field from other atmospheric and surface factors so that more direct estimates of the radiative effects of clouds can be made. Moreover, the modeling approach also allows us to partition the TOA radiation budget

into its surface and in-atmosphere components in a self-consistent manner (Rossow and Lacis 1990).

Comparison between the model calculated OLR from ISCCP retrieved cloud properties, supplemented by other atmospheric and surface datasets, and the ERBE OLR shows that while the two fluxes agree reasonably well in general, systematic differences exist in specific locations suggesting particular local surface, atmospheric and cloud conditions are responsible for the disagreement between these two products (Rossow and Zhang 1995; Xu 1997). It is imperative to identify the sources of these discrepancies, because these systematic differences, though relatively small in magnitude, are certainly significant when compared with the radiation budget changes that appear interannually or that are being considered in relation to possible climate changes induced by changes in atmospheric composition (increasing abundance of greenhouse gases and aerosols) and, consequently, cannot be ignored in evaluating the effects of cloud-radiation interactions on the climate. Identifying the sources of discrepancies will also help to identify the problems associated with the two approaches. Unfortunately, examining and isolating the sources of disagreement is complicated by the effects of different temporal and spatial sampling of the ISCCP and ERBE measurements.

The existence of both narrowband and broadband channels on the ScaRaB radiometer provides a unique opportunity to compare the narrowband-based ISCCP and broadband-based ERBE approaches using coincident, collocated, and coangular radiance measurements and flux estimates. The narrowband channels of ScaRaB are roughly equivalent to the visible and infrared channels used in the ISCCP cloud retrievals, while the broadband channels are similar to those of the ERBE scanners. Thus, it is possible to use the ScaRaB data to retrieve the OLR using the ISCCP approach with the narrowband radiances and using the ERBE approach with the broadband radiances. Use of the ISCCP-like and ERBE-like OLRs from the ScaRaB measurements eliminates the uncertainties due to the temporal and spatial mismatches and allows us to focus on the differences between the ISCCP and ERBE approaches which is invaluable for the validation and improvement of both approaches and will significantly advance our understanding of ERB as a consequence. Particularly, simultaneous narrowband and broadband measurements allow us to

isolate the effects of angle model differences in the analyses[1]. Since our comparisons are restricted to the instantaneous pixel-level radiance and flux values, the differences in the space-time averaging algorithms used to obtain proper averages of the fluxes from temporally and spatially sparse samples are not considered in this study. There are other studies designed for this purpose (e.g., Xu 1997). Moreover, this particular study is only intended to identify the sources of disagreements in the ERBE and ISCCP approaches. The radiative effects of clouds using ISCCP and ERBE data are the subjects of other research efforts (e.g., Harrison et al. 1990; Hartmann and Doelling 1991; Ockert-Bell and Hartmann 1992; Hartmann et al. 1992; Chen et al. 2000a,b).

A short description of the ScaRaB project and its ERBE-like inversion method is given in Section 2. The ISCCP approach to determine OLR using the ScaRaB narrowband radiances is described in Section 3. Section 4 relates the cloud cover categories from the broadband-based ERBE maximum likelihood estimation technique to the cloud types from the narrowband-based ISCCP cloud detection and retrieval algorithm. Section 5 examines the differences between the ISCCP-like and ERBE-like OLRs as a function of ISCCP cloud parameters and discusses the possible sources of disagreements. Section 6 summarizes the main findings and discusses the implications of this study.

[1] The unique advantages for addressing angular model related issues provided by ScaRaB have also been exploited in the study by Chang et al. (2000b), which focused on the TOA albedo and SW angular dependence models.

2. ScaRaB project and inversion method

a. ScaRaB project

The Scanner for Radiation Budget (ScaRaB) project is a joint project of France, Russia, and Germany intended to provide a continuation of the ERBE scanner mission (Kandel et al. 1994). The first ScaRaB flight model (FM1) was launched on board the Russian *Meteor-3/7* weather satellite with circular polar orbit at an altitude of 1200 km and an inclination of 82.5° (not sun-synchronous). The orbit plane precessed relative to the sun-earth vector with a period of approximately 213 days, resulting in full coverage of the diurnal cycle in about 106 days. The ScaRaB instrument is a cross-track scanning radiometer with a swath of 97.82° (i.e., the maximum satellite nadir angle is 48.91°, yielding a maximum viewing zenith angle of 63.57° considering the curvature of the earth; Capderou 1998). The angular resolution of instantaneous field of view is 48 x 48 $mrad^2$, corresponding to a pixel size of 60 x 60 km^2 at nadir. The radiometer consists of two narrowband and two broadband channels with identical fields of view. The two narrowband channels are similar to the weather satellite imager channels used in the ISCCP analysis, one corresponding to visible portion of the solar spectrum (VIS: 0.55-0.65 μm), the other to the infrared atmospheric window (IRW: 10.5-12.5 μm). The broadband shortwave (SW: 0.2-4 μm) and total radiation (TW: 0.2-50 μm) channels of ScaRaB, from which the reflected shortwave and emitted longwave radiances are derived, are analogous to those of the ERBE scanner. Daytime radiation in the longwave band (LW: nominally 4-50 μm) is obtained by appropriated weighted subtraction of the SW signal from the TW signal. The radiometric accuracy of the radiances is estimated to be better than 1% in the LW and 2% in the SW domains. The data was received and processed from 24 February 1994 until 6 March 1995 with some interruptions; therefore, roughly 11 months of data has been collected (Kandel et al. 1998).

b. Inversion method

As a follow-on of ERBE, the first version of the ScaRaB data processing was developed as an "ERBE-like version" to ensure consistency between ERBE and ScaRaB products. In other words, the ScaRaB algorithms are as close as possible to the ERBE algorithms except for some

parameters used in ERBE scene identification, which are missing in the published descriptions of ERBE (Viollier et al. 1995)[2], and the steps specific to the instrument characteristics, such as the spectral corrections. Like all scanning radiometers, ScaRaB measures radiances at specific angles. The filtered SW and LW radiances, after radiometric calibration, are first corrected for spectral filtering effects. Spectral correction is in general a function of scene type. For the ScaRaB LW radiance, which is the result of weighted subtraction of the SW from the TW channels, however, the filtering error is negligible and therefore no spectral correction is applied in the current ScaRaB inversion process (Viollier et al. 1995). The ERBE angular dependence models (ADMs), which account for the anisotropy of the radiation field, are then applied to the unfiltered SW and LW radiances to obtain the SW and LW fluxes at TOA (Suttles et al. 1988; Suttles et al. 1989).

Since the angular dependence models depend on the type of surface and the amount of cloud present in the observed scene, a procedure is required to identify the scene type. The algorithm of scene identification is the maximum likelihood estimation (MLE; Wielicki and Green 1989), which compares the unfiltered LW and SW radiances to a priori statistics developed from a classification of *Nimbus-7* ERB data. The 12 scene classifications are the same as used by ERBE, based on a combination of five geotypes (ocean, land, snow, desert, coast) and four cloud categories: clear [0%-5% cloud cover], partly cloudy [5%-50% cloud cover], mostly cloudy [50%-95% cloud cover], overcast [95%-100% cloud cover]. Very roughly, the MLE expects a clear scene to be dark and hot, cloudy scenes to be bright and cold. Presumably, the larger pixel size of ScaRaB (60 km at nadir, versus 30-45 km for ERBE) should give rise to a different scene type distribution compared with ERBE. This effect, however, is mitigated because the a priori probabilities used in the ScaRaB scene identification were computed by analyzing the scene fractions of the ERBE S-9 archive (Viollier et al. 1995). Since the objective of the ScaRaB project is to determine the TOA ERB components on a scale appropriate to the study of cloud radiation interactions, an additional procedure is performed to obtain proper averages of the fluxes from

[2] Several improvements are being planned for the future version of ScaRaB data processing, including adapting ISCCP cloud detection algorithms to the coarse spatial resolution of the ScaRaB narrowband measurements for better scene/cloud identifications and thus improved clear-sky fluxes and cloud radiative effects (Briand et al. 1998) and applying different angular dependence models from recent studies for the conversion of radiances into fluxes (e.g, Stubenrauch et al. 1993).

temporally and spatially sparse samples (Brooks et al. 1986). However, as mentioned before, the problems associated with the spatial and temporal averaging algorithms are beyond the scope of this present study, since our results are restricted to the instantaneous pixel-level radiance and flux values.

Similar to ERBE, three levels of ScaRaB data are produced by the data processing procedures. In particular, the second level (A2) is directly comparable to the ERBE S-8 product containing instantaneous unfiltered SW and LW radiances, estimated TOA fluxes, as well as scene identifications at the pixel level, and is the primary data source for this study (Kandel et al. 1998).

3. ISCCP-based approach for OLR determination

The ScaRaB visible (VIS) and infrared window (IRW) channels are comparable to those used in the ISCCP analysis; thus it is a natural idea to apply the ISCCP algorithm to the ScaRaB VIS and IRW radiances. Similar to many cloud algorithms, the ISCCP algorithm consists of two basic phases: the cloud detection phase and the cloud properties derivation phase. Based on a series of statistical analyses of the radiance variations, the cloud detection algorithm first infers the clear-sky VIS and IRW radiances for each individual pixel. An individual pixel is then classified as cloudy, if either the VIS or IRW radiance differs from its corresponding clear-sky value by more than the detection thresholds, or clear if otherwise (Rossow and Garder 1993a). If the pixel is cloudy, then comparison of the observed radiances to those predicted by a radiative transfer model determines a cloud top temperature (T_c) from the IRW radiance and a visible optical thickness (τ, daytime only) from the VIS radiance. If the pixel is clear, then surface temperature (T_s) and surface visible reflectance (R_s, daytime only) are retrieved (Rossow et al. 1996). The effects of the atmosphere on the radiances are accounted for and cloud top pressure (P_c) is determined from T_c using the atmospheric temperature and humidity profile from the Television Infrared Observation Satellite (TIROS) Operational Vertical Sounder (TOVS) product (Kidwell 1995). To be consistent with the cloud and surface retrieval, the same TOVS profile is also used in the radiative transfer model calculation in this study (unless otherwise indicated).

From the ScaRaB VIS and IRW radiances, cloud and surface properties are retrieved in the same form as the ISCCP DX (pixel level). The ScaRaB-derived cloud and surface properties, called ScaRaB DX, are then combined with ancillary data and used as input to a radiative transfer model to calculate fluxes. The radiative transfer model is a refined version of the one described by Zhang et al. (1995) with similar input and output quantities. The improvements most relevant to this study are as follows. 1) The clouds are treated using an ice microphysical model if top temperature < 260 K, which is consistent with the ISCCP retrieval. 2) The spectral resolution of k-distribution method is increased from 25 to 33 k-intervals for thermal radiation (Lacis and Oinas 1991). 3) The parameterization of water continuum absorption is improved using the theoretical calculations by Ma and Tipping (1991, 1992a,b). 4) Non-unit-emissivity is used for the surface

with correction of the retrieved surface skin temperature. 5) Better interpolation for surface air temperature is introduced.

For the LW radiation, which is the focus of this study, the radiative transfer model uses a three-point quadrature (corresponding to emission angles of $cos\theta$ = 1.0, 0.5, and 0.1) to integrate over the angular distribution of the radiation (Lacis and Oinas 1991). A by-product of this added complexity is that we have available from the radiation model an infrared window radiance, a spectrally integrated broadband radiance (both for nadir-viewing geometry and also for the more extreme emission angles of $cos\theta$ = 0.5 and 0.1), and angle-integrated fluxes. Thus, the radiative transfer model can be used to simulate the narrowband and broadband ScaRaB measurements for direct comparison with the measured radiances, as well as allowing comparison of the resulting fluxes (Fig. 1). This aspect of the radiative transfer model makes the ISCCP approach well-suited to examine the effect that changing cloud properties have on the determination of ERB fluxes.

Although all 11 months of ScaRaB FM1 narrowband radiance data have been processed through the ISCCP cloud algorithm, our analyses are performed on only two months of ScaRaB DX data since, typically, one month of ScaRaB DX data consists of several million observations and hence are enough to produce statistically significant results. However, since the satellite retrieval and flux calculation/conversion also depends on the relative geometry among sun, Earth target, and satellite, we choose two specific months, namely May and July 1994, to provide a representative sample of sun-target-satellite geometries. In May 1994, the daylight Equator Crossing Time (ETC) of the satellite was around early afternoon, drifting from about 1500 local time (LT) at the beginning of the month to about 1200 LT at the end of the month. Because of the precession of the orbit, the daylight ETC changed to early morning in July 1994, varying from 0900 to 0700 LT approximately. Only the daytime observations are used in this study, since both approaches are more accurate for the daytime than for the nighttime observations due to the fact that, lacking visible information, both the ISCCP cloud detection and the ERBE MLE scene identification algorithms degrade into single threshold tests for the nighttime observations. Besides, in the ISCCP retrieval, cloud optical thickness is determined from visible radiance measurements, which are only available during daytime, and the cloud top temperature is more

accurately determined as a function of optical thickness (Rossow et al. 1996; Rossow and Schiffer 1999).

One of the problems encountered when applying the ISCCP algorithm to the ScaRaB measurements arises from the coarse spatial resolution of ScaRaB measurements (60 km at nadir), since the ISCCP algorithm is optimized for use with pixel size of 4-7 km. Differences in the pixel size primarily affect the retrieval in two ways. 1) The spatial and temporal variability of the surface characteristics decreases as the pixel size increases. This will cause some cloud-contaminated ScaRaB pixels to be declared clear by the original ISCCP cloud detection algorithm, where the thresholds in the space/time variability test are selected for use with higher spatial and temporal variations of radiances associated with the finer spatial resolutions (Briand et al. 1998). 2) ISCCP assumes that the cloud optical properties are uniform at pixel scales; hence, the cloud cover of pixels is assumed to be either zero or one. This assumption becomes less acceptable at the lower ScaRaB spatial resolution. To separate the clear (cloudy) ScaRaB DX pixels with minimal cloud (clear-sky) contamination from the clear (cloudy) pixels with possible cloud (clear-sky) contamination, the ScaRaB DX pixels are compared with the actual ISCCP DX pixels matched in both space and time as closely as possible. The comparison divides the matched ScaRaB DX pixels into two subsets, called "unmixed" and "mixed". The clear (cloudy) ScaRaB DX pixel is classified as "unmixed" only if its four nearest (within a radius of 60 km)[3] neighboring ISCCP DX pixels are all labeled as clear (cloudy) and is classified as "mixed" otherwise. For the "unmixed" pixels, we assume that when four nearby ISCCP DX pixels are clear (cloudy), the whole region of ScaRaB DX pixel is entirely clear (cloudy). Conversely, the "mixed" pixels are more likely to be partially cloud covered. On average, about 65% of the matched clear (determined by ISCCP analysis) ScaRaB DX pixels are labeled as "mixed", indicating that a quite large portion of the ISCCP-declared clear ScaRaB pixels may actually contain small amount of clouds to compensate for the effects of the lower spatial resolution, as pointed out by Briand et al. (1998). A large

[3] Since the ScaRaB pixel size grows to over 200 km at 60° view, limb-viewed ScaRaB pixels should be compared with significantly more neighboring ISCCP DX pixels in theory. However, if more ISCCP DX pixels were used, the number of "unmixed" pixels would have decreased significantly. To retain enough "unmixed" pixels for analysis, four nearest ISCCP DX pixels are used regardless of the ScaRaB viewing angle. As a result, a portion of limb-viewing "unmixed" ScaRaB pixels are in reality "mixed". The consequences are considered later in Section 5.

majority (about 75%) of the ISCCP-declared cloudy ScaRaB pixels are labeled as "unmixed" rather than "mixed", especially for the cloud types that are optically thick or of large size such as deep convective or cirrostratus clouds (see Fig. 2 for the ISCCP radiometric cloud classification). The only exception arises for the ScaRaB pixels determined as cumulus by the ISCCP algorithm, where more than half (roughly 58%) of them are labeled as "mixed", consistent with the facts that 1) cumulus clouds tend to be small-sized and broken; and 2) partially-filled cloudy pixels are more likely classified as cumulus rather than any other cloud type in the ISCCP analysis. Although completely clear or overcast does not imply that the optical properties of surface or cloud are uniform over areas of tens of kilometers, the assumption of optical homogeneity is certainly a better one for the "unmixed" pixels than for their "mixed" counterparts. It is therefore interesting to contrast the results from the "unmixed" pixels with those from the "mixed" ones and examine to what extent the results are affected when this assumption is severely violated, as will be done in section 5.

4. Relationship of MLE cloud cover categories to ISCCP cloud types

In the ERBE MLE, the full range of observed cloud height and optical thickness variations are only implicitly included in the derived cloud cover categories (Wielicki and Green 1989). ISCCP cloud detection and classification, on the other hand, attributes all variations in the narrowband radiances to changes in cloud top temperature and visible optical thickness, assuming clouds cover individual pixels completely. Examination of the MLE-derived cloud cover categories within the context of ISCCP-derived cloud types, defined by the cloud top pressure and visible optical thickness (Fig. 2), will not only allow us to better understand the MLE-derived cloud cover, but also help us to explain the differences between the ERBE- and the ISCCP-approach radiative fluxes.

Tables 1 and 2, respectively, give the May 1994 monthly global results of the distribution of the ISCCP-derived scene types in each of the four MLE-derived cloud cover categories and the distribution of the four MLE-derived cloud cover categories in each of the ISCCP-derived scene types. The ISCCP-derived global mean ScaRaB cloud amount (62.9%), defined as the percentage of cloudy pixels, is about 5% lower than the 8-yr (1986-93) global mean cloud amount of the actual ISCCP D-series data (67.6%, Rossow and Schiffer 1999). Since the ScaRaB spatial resolution is much lower than the original ISCCP resolution, this result strongly indicates that the ISCCP algorithm is quite stable with spatial resolution variations, as also observed by Briand et al. (1998). Compared with the ISCCP-derived ScaRaB clear-sky amount (37.1%), the MLE-derived ScaRaB clear-sky amount is about 11% less (Table 2). This is not unexpected since, on the one hand, the original ISCCP algorithm, when applied to the coarser ScaRaB measurements, tends to overestimate the clear-sky amount by misidentifying some cloud-contaminated pixels as clear (Briand et al. 1998) and on the other hand, the MLE clear-sky amount is biased low because the definition of clear sky in the ERBE analysis is overly restrictive (Collins and Inamdar 1995). For the ScaRaB pixels declared as clear by the ISCCP cloud detection algorithm, more than half of them are also labeled as clear by the MLE scene identification scheme, and less than 10% of them are labeled as overcast by MLE.

However, the most distinctive feature shown in Table 1 is the progressively higher MLE-derived cloud cover for the ISCCP-derived cloudy pixels with larger optical thickness or lower top pressure values because of the stronger solar or thermal contrast between these clouds and clear sky, consistent with Diekmann and Smith (1989). This dependence implies that the MLE-derived cloud cover is likely to be biased low for low thin clouds and biased high for high opaque clouds. In other words, the MLE-derived cloud cover will best approximate true cloud cover for clouds with average height and optical thickness, since the a priori data used by the MLE is an average over all observed cloud heights and optical thicknesses, as pointed out by Wielicki and Green (1989). Specifically, for the ScaRaB pixels classified as cumulus by ISCCP, characterized by their relatively weak radiative contrast from clear sky, they are most likely classified as partly cloudy by MLE. For the ScaRaB pixels classified as stratocumulus, stratus, altocumulus, or altostratus by ISCCP, the MLE scene identification most likely declares them as mostly cloudy. This result is consistent with Chang et al. (2000a), who also find that nearly all of the uniform low-level, single-layered, marine overcast clouds (based on the spatial coherence analysis applied to AVHRR measurements) were classified as mostly cloudy by ERBE MLE. Finally, for the ScaRaB pixels classified as cirrus, nimbostratus, cirrostratus, or deep convective cloud by ISCCP, most likely they are declared to be overcast in the MLE, showing that the MLE method expects the overcast pixels to be both cold and bright by design. Overall, for the ScaRaB pixels declared as cloudy by ISCCP, the MLE method most likely classifies them into mostly cloudy scenes.

In the MLE classification, for May 1994, the ScaRaB pixels are roughly evenly distributed among the four MLE cloud cover categories, where the difference between highest and lowest frequency of occurrence (FOC) is less than 9% (Table 2). Among the ScaRaB pixels classified as clear by MLE, more than 80% of them are also declared clear by ISCCP. For the ScaRaB pixels classified as partly cloudy by MLE, more than 90% of them are declared either clear sky, low clouds with thin or medium optical thickness (cumulus and stratocumulus), or thin middle-level clouds (altostratus) by ISCCP. For the MLE-derived mostly cloudy and overcast ScaRaB pixels, the ISCCP algorithm tends to classify them as clouds with even larger optical thickness and/or lower top temperature. Again, this table shows that the ERBE MLE-derived cloud cover implicitly

includes information on cloud height and optical thickness, producing mixtures of τ-variation and P_c-variation. Since the ERBE ADMs are empirically constructed by sorting the *Nimbus-7* ERB measurements into latitude bins, angular bins and cloud cover categories, it is anticipated that for each particular cloud cover category, the associated angular model tends to be biased to the angular behavior of the ISCCP scene types with the highest FOCs. The most likely scene types, however, may differ from the ones in this study, since the cloud detection algorithm used to construct the ERBE ADMs was the new cloud-ERB (NCLE) algorithm (Stowe et al. 1988) and significant differences exist in cloud fraction between the MLE and NCLE results (Suttles et al. 1992). It is worth noting that considerable differences in cloud fraction exist between the ISCCP and NCLE results, too (Rossow et al. 1993).

A closer look at the two classifications reveals that the relation between ISCCP- and MLE-derived scene types varies with the satellite viewing zenith angle (VZA). Figure 3, showing the variation of MLE-derived scene type frequency of occurrence (FOC) as a function of VZA (grouped by ISCCP-determined scene types) for May 1994, reveals that the MLE scene type FOC varies considerably with the satellite viewing angle for some particular ISCCP-derived cloud types. Most notably, for the ScaRaB pixels identified as cirrus by ISCCP, the FOC of overcast in the MLE increases from about 20% for VZA = 0°-15° to over 40% for VZA > 51°. This considerable variation may result from the viewing angle dependence of MLE scene identification scheme (Ye and Coakley 1996a,b) or from that of ISCCP cloud detection and retrieval algorithm (Rossow and Garder 1993b), but more likely from both. The viewing angle dependence of MLE implies that the two steps used in the ERBE approach to derive the radiative fluxes, that is, first identifying within each scanner field of view the scene type, then applying an anisotropic factor associated with that scene type to convert radiances into fluxes, are intricately linked to each other and should not be viewed separately. When the entire population of pixels is included, however, no viewing angle dependence is apparent in the MLE scene type FOC (except for a very slight decrease in clear scene FOC as VZA increases) regardless of the month considered. In reality, since the ScaRaB field of view size grows with the viewing zenith angle, from ~60 km at nadir to over 200 km at limb, one would expect that FOC increases for partly and mostly cloudy scenes

and decreases for clear and overcast scenes. This is not the case in Figure 3, which suggests that the scene type names used by the MLE classification are rather inexact and misleading, and hence should not be interpreted literally. Similar results are also obtained for the near-terminator month, July 1994 (not shown).

5. Comparison between the two approaches

As discussed earlier, both the ISCCP retrieval algorithm and radiative transfer model for the flux calculation assume optical homogeneity in the underlying pixels. Undoubtedly, this assumption becomes increasingly a problem as the pixel size increases. To alleviate this problem associated with the relatively coarse spatial resolution of ScaRaB measurements, we will first restrict the results to the "unmixed" scenes. Then the results from the "mixed" scenes will be briefly discussed to determine how the results are affected when the optical homogeneity assumptions are severely violated. Apart from the above mentioned optical homogeneity issue, our comparisons are complicated further by the following two differences between the ERBE and ISCCP approaches. 1) The TOA is chosen as 30 km in the ERBE analysis, whereas the model calculations set TOA as 100 km. Using 30 km instead of 100 km as the definition of TOA in the radiative transfer model produces a fraction of a percent difference in the calculated radiances or fluxes. 2) The synthetic ScaRaB LW channel (the result of weighted subtraction of the SW from the TW channel) has a nominal spectral range from 4 to 50 μm, whereas the model calculated LW radiance or flux represents the range from 5 to 200 μm. This difference may cause a low bias of as much as 1% in the ScaRaB LW measurements.

a. "Unmixed" pixels

Figs. 4a and 4b show the mean differences (over ocean, "unmixed" pixels only) between the measured and model-simulated TOA LW radiances, between the converted TOA LW fluxes using measured LW radiances (results from two different ADMs, called ERBE and SDK ADMs — see later text for details) and model calculated fluxes for May and July 1994, respectively. Similar results are obtained over land (not shown). Results from clear and cloudy, from nadir- and limb-viewing pixels (VZA = 0^{o} and 60^{o}) are separately presented. Cloudy pixels are further grouped into 15 classes according to the ISCCP retrieved cloud top pressure (separated at 680 mb and 440 mb) and optical thickness (divided at 1, 3.6, 9.4, and 23). Except for the clear and low cloud cases, where the differences exhibit a simple latitudinal dependence (maximum in the Tropics), the differences are generally independent of the geographical location, and hence only

the global mean results are discussed (likewise the numbers quoted in the text, unless otherwise noted). Figs. 5a and 5b are similar to Figs. 4a and 4b, except that only the pixels where the measured and model-simulated LW radiances agree to within 0.5 $Wm^{-2}sr^{-1}$ are included, so that the LW flux difference can originate only from the difference between the ADMs used by the ERBE-like approaches and the radiative transfer model's treatment of the angle integration.

i. Clear sky and low clouds

Even for the "unmixed" clear ScaRaB DX pixels, a significant portion of them (26.2% for May 1994, and 44.0% for July 1994) are identified as somewhat cloudy by the ERBE MLE method. To minimize the uncertainties in clear-sky results caused by the possible cloud contamination, only the clear "unmixed" pixels where both ISCCP and MLE agree are included in the comparison. Averaged over the globe, the clear-sky TOA LW fluxes estimated from the observed LW radiances and ERBE ADMs always exceed the model calculations, ranging from ~3 Wm^{-2} for limb-viewing (VZA = 60°) land pixels of July 1994 (not shown), to ~14 Wm^{-2} for nadir-viewing ocean pixels of May 1994. Note that the high bias in the ERBE analysis shown here cannot be explained by the conventional wisdom that the ERBE clear sky TOA LW fluxes are biased high, especially in the Tropics, due to the overly restrictive clear sky definition in the ERBE analysis (cf. Hartmann and Doelling 1991; Collins et al. 1995) for the following two reasons: 1) the current flux comparison is made on the same "unmixed" clear pixels where ISCCP and MLE agree; and 2) these "unmixed" clear pixels, by definition, tend to be found in the midst of vast regions that are clear, and thus are highly unlikely to be cloud-contaminated. In light of the fact that ERBE ADMs do not explicitly take into account the attenuation of LW radiation by the atmosphere above the surface or cloud top, Stubenrauch et al. (1993) parameterized the longwave ADMs using combined narrowband IRW and broadband LW observations to specifically include the effects of cloud height variations (referred to as SDK ADMs in this paper). Replacing the original ERBE ADMs with the SDK ADMs only slightly reduces the discrepancy in the clear sky TOA LW fluxes. The comparison between the observed and model-simulated LW radiances shows that the flux differences largely arise from the disagreements in the broadband radiances.

This is further confirmed in Figs. 5a and 5b. For the clear pixels where the measured and simulated radiances agree, the flux differences between radiance converted (using either ERBE or SDK ADMs) and model calculated fluxes are very small (in the worst case 2.5 Wm^{-2}), indicating that these two ADMs (especially the ERBE ADMs) and the radiative transfer model's representation of longwave emission anisotropy are fairly similar for clear conditions.

A detailed investigation of this clear sky difference shows that there is a positive correlation between the LW radiance differences (observation minus calculation) and the column precipitable water amount (Fig. 6). Considering the sensitivity of the radiative transfer model to the input atmospheric temperature and humidity profiles, we repeated the calculations using the atmospheric profile from the TOVS Pathfinder path-B dataset (hereafter 3I profile, from the name of the retrieval algorithm used; Scott et al. 1999). The use of 3I profile brings the simulated LW radiances closer, in a global mean sense, to the observations by 1-2 $Wm^{-2}sr^{-1}$, leading to a 3-6 Wm^{-2} reduction in the flux difference; however, a stronger correlation between LW radiance differences and the column precipitable water amount is observed, regardless of the month and viewing zenith angle, implying a larger difference between the ADM-derived and model calculated latitudinal gradients of radiative fluxes using the 3I than the TOVS profile. Note that this result does not necessarily suggest that the water vapor itself (either the errors in the input humidity data or the treatment of water vapor in the model) is the source of the discrepancy, because other properties of the atmosphere that affect longwave radiation (such as temperature) are highly correlated with water vapor.

We have repeated the radiative transfer calculation by adjusting several model inputs to which the TOA longwave radiation is most sensitive, such as increasing the atmospheric or surface temperature, or reducing the atmospheric humidity within their assessed uncertainty ranges (cf. Zhang et al. 1995). Though each of the adjustments brings the model calculation closer to the observation, none of them is, by itself, sufficient to explain the large discrepancy between model calculation and observation for the nadir-viewing ocean pixels of May 1994. It is likely that the discrepancy arises as a combined result of uncertainties in the model inputs and/or errors in the radiative transfer model. However, since very different amount of changes to the model inputs are

needed to get agreement between model calculations and observations in May and July, the discrepancy in LW radiances/fluxes may be due more to uncertainties in the model inputs than to errors in the radiative transfer model. Those uncertainties/errors need to be investigated and quantified with further research.

Similar to the clear-sky results, but at a reduced magnitude, both the observed LW radiances and the radiance-converted fluxes exceed the model calculations for the ScaRaB pixels identified as containing low clouds ($P_c > 680$ mb) by ISCCP (regardless of the MLE-derived cloud cover), due mainly to the clear-sky effect. Figure 5 shows that the TOA LW flux differences for low clouds stemming from the different angle treatments are generally very small as well, despite a weak but systematic dependence on optical thickness and viewing zenith angle. Similar but stronger dependencies are also observed for middle- and high-level clouds, which will be discussed next.

ii. High- and middle-level clouds

As shown in Figs. 4a and 4b, for the ScaRaB pixels classified as high clouds ($P_c \leq 440$ mb) by ISCCP, the model-simulated LW radiances can be either less or greater than the observed ones, depending on the retrieved optical thickness and viewing zenith angle. When the clouds are very optically thin, the model in general underestimates the TOA LW radiance. At nadir-viewing geometry, the difference is about 4 $Wm^{-2}sr^{-1}$. Analysis shows that the bias primarily arises from the visible adjustment procedure in the ISCCP retrieval. ISCCP first retrieves the cloud top temperature assuming that the cloud is opaque to infrared radiation, then adjusts the retrieved cloud top temperature if the infrared transmission of the cloud estimated from the retrieved visible optical thickness is greater than 0.5%[4]. This procedure encounters difficulties with very thin clouds because the errors in the optical thickness, surface temperature, and the ratio used to relate the optical thickness value in the VIS to that in the IRW will be greatly amplified when the

[4] A small coding error in the ISCCP visible adjustment step that causes a slight overestimation of cloud top temperature and pressure for clouds with visible optical thickness between 2 and 6 has been found. This error has been corrected for the ScaRaB DX data used in this study and for the regular ISCCP D data for 1994 and later. However, ISCCP D data for July 1983 through 1993 still contain this error (see appendix).

infrared transmission is too large. Thus, for the clouds with $\tau cos\theta < 1.2$, ISCCP tends to place them at the tropopause and reset the optical thickness to a proper value so that the infrared window (but not the VIS) radiance is preserved (Rossow et al. 1996). This treatment inevitably leads to a cold bias in the calculated broadband longwave radiance, due to the different cloud-radiation interactions inside and outside the infrared window wavelength range: even though the combination of T_c and τ reported by ISCCP matches the radiation in the window, if the clouds are too high they reduce the radiation outside the window too much.

As for the high clouds with medium or large optical thickness, the model-simulated LW radiances agree rather well with the observations for nadir-viewing pixels, but always exceed the observations for pixels with VZA = 60°. Noticing that the agreement is worse for the "mixed" pixels (cf. Fig. 8), we speculate that the larger discrepancy at 60° view is caused, at least in part, by forcing the ISCCP analysis (optimized for use with pixel size of 4-7 km) to operate on the excessively large limb-viewing pixels that tend to have a larger degree of sub-pixel cloud heterogeneity and brokeness (even for the "unmixed" pixels). In fact, we have repeated the analysis by comparing the ScaRaB DX pixels with the 16 nearest ISCCP DX pixels (within a radius of 200 km, roughly the size of limb-viewing ScaRaB pixel) and found that more than half of the original "unmixed" ScaRaB DX pixels are no longer "unmixed". For those ScaRaB pixels that remain "unmixed", the standard deviation of cloud top temperatures over the 16 neighboring ISCCP DX pixels (σ_{T_c}) is computed and used as the indicator of sub-pixel cloud heterogeneity within each individual ScaRaB DX pixel (cf. Stubenrauch et al. 1993). We found that both the mean and standard deviation of the discrepancy between the model-simulated and observed LW radiances at 60° view decrease as σ_{T_c} gets smaller (Fig. 7).

Overall, the model-simulated radiances agree better with the measurements for the middle-level clouds (440 mb < $P_c \leq$ 680 mb). However, this agreement is more likely due to the cancellation of two opposing effects, namely the "clear sky" bias (mostly affecting clear sky and low clouds) and "sub-pixel cloud heterogeneity/brokeness" effects (mostly affecting limb-viewed high clouds), with both effects operating at a smaller magnitude. As a result, the vertical

distribution of the longwave cooling and surface radiation might not be correctly simulated, even if the TOA radiation is correctly calculated for the midlevel clouds.

iii. ERBE and SDK ADMs and the model's treatment of angle integration

The fact that the differences in ADM-converted and model calculated flux only approximately follow the radiance differences suggests that part of the flux differences are caused by the difference between the ADMs used and the radiative transfer model's treatment of angle integration. Although the relative contribution of the different angle treatments to the flux differences is difficult to determine exactly, Figs. 5a and 5b do provide some insight.

We first consider the ERBE ADMs. It is observed in both Figs. 5a and 5b that for the nadir view, when the observed and the model-simulated radiances agree, the ERBE ADM converted fluxes are higher (lower) than the model calculated ones for clouds with small (large) optical thickness, regardless of the cloud height. The opposite is true for the 60° view. This indicates that, compared with the radiative transfer model, the limb-darkening in the ERBE angular models is too weak for the optically thin clouds ($\tau < 3.6$), but too strong for the optically thick clouds ($\tau > 9.4$). When all clouds are included, however, the limb-darkening in the ERBE angular models closely resemble that implied by the radiative transfer model (not shown). In reality, for clouds at the same height, optically thin clouds usually are more limb-darkened than the optically thick clouds. For instance, due to the $sec\theta$ dependence of radiation path length through the cloud layer, optically thin cirrus can be nearly transparent to LW radiation at near nadir viewing angles, while the same cloud can be nearly opaque to LW radiation at near-limb viewing angles, leading to the limb-darkening even stronger than that for clear-sky conditions (Wielicki and Green 1989). On the other hand, the optically thick clouds are usually more Lambertian compared with clear scenes. These results suggest again that the ERBE ADMs represent the anisotropy of the LW radiation averaged over all cloud types but not for particular cloud types. This is not surprising considering that the ERBE ADMs are based on a large set of *Nimbus-7* ERB observations without explicit distinction of different cloud optical properties. As pointed out by Stubenrauch et al. (1993), if the dependence of angular models on the cloud properties was not taken into account in their

construction, it must be averaged out in the final products. In fact, this is exactly what happened, since the longwave ERBE ADMs are all quite similar with angle variations of only 1% to 2% on average among the four cloud conditions (Suttles et al. 1989). Also notice from Figs. 5a and 5b that the difference between the ERBE ADMs and the angle treatment of the radiative transfer model increases with cloud height. As a result, the differences in the estimated fluxes caused by the different angle treatments between the ERBE and ISCCP approaches are not the same for the low as for high clouds. This is very important since the radiative flux gradient, one of the ultimate forcings driving the atmospheric circulation, between the climate regimes characterized by persistent but different cloud types is not equally represented by these two approaches. Yet, this difference in the gradient cannot be completely eliminated in the final space- and time-averaged products, as will be discussed in the next section.

Figs. 5a and 5b show that for the optically thick clouds ($\tau > 9.4$), the SDK ADMs and the radiative transfer model's angle treatment are very similar. This is anticipated since the SDK ADMs are developed on the basis of radiative transfer calculations assuming a horizontally homogeneous surface or cloud layer of unit emissivity (Stubenrauch et al. 1993). Interestingly, for the optically thin clouds, the SDK ADMs appear to coincidentally behave more like the ERBE ADMs.

b. "Mixed" pixels

Figs. 8 and 9 are the same as Figs. 4a and 5a, respectively, except they show results for the "mixed" pixels. For high-level broken cloud fields, the agreement between model-simulated and observed LW radiances deteriorates. However, this effect is rather small on the global scale considering the relatively infrequent occurrence of high-level broken cloudiness: high clouds, usually large in size, tend to be continuous over a large area. In fact, the majority of the broken cloudiness is confined to the low level, small cumulus clouds in the trade wind regimes. For mid- and low-level clouds, the patterns shown in Fig. 8 are very similar to those in Fig. 4a, indicating that the uncertainties in the estimated TOA longwave radiation budget caused by broken cloudiness are quite small, even at the coarse spatial resolution of ScaRaB. This can be explained

by the cancellation of two offsetting effects. In the presence of broken cloudiness, the radiance used to retrieve the cloud is an averaged value from the actual clouds and surface, hence, the retrieved cloud assumed to cover the entire pixel is on average lower and optically thinner than the actual clouds. The larger cloud cover tends to decrease the longwave radiation whereas the higher cloud top temperature and smaller optical thickness tend to increase the longwave radiation. In the low cloud cases, the effect of broken cloudiness on the TOA longwave radiation budget is even smaller because the TOA longwave radiation is largely determined by the atmosphere above the clouds.

6. Summary and discussions

Two conceptually different approaches (broadband-based ERBE and narrowband-based ISCCP approaches), used to derive the TOA longwave radiative fluxes, are compared using the ScaRaB simultaneous narrowband and broadband measurements (cf. Fig. 1). To evaluate the ERBE scene identification algorithm and facilitate the flux comparisons, the ERBE MLE-derived scene types are first compared with the ISCCP-derived cloud types on a pixel-by-pixel basis. The comparison shows a progressively higher MLE-derived cloud cover for the ISCCP-derived cloudy pixels with larger optical thickness or colder top temperature, indicating the cloud properties are implicitly included in the derived cloud cover categories (cf. Wielicki and Green 1989). Moreover, the comparison also confirms a view-zenith angle dependence of the MLE scene identification scheme (cf. Ye and Coakley 1996a,b), which could mean that the ERBE ADM converted radiative fluxes can be erroneous even if the ADMs themselves are correct, because they are not selected correctly at all viewing angles. But in reality, the errors in the scene identification scheme are more likely offset to some extent by the errors in the ADMs if the same scene identification scheme is used in the development and application of ADMs (Chang et al. 2000a). Thus, the scene identification and radiance-to-flux conversion steps in the ERBE processing are intricately linked together and should not be viewed separately.

For the clear sky, the model underestimates the observed TOA LW radiances on the global average. Though the bias is found to be correlated on the column precipitable water amount, the exact source of the bias remains undetermined because of the possible dependencies on other variables, most notably temperature, that are correlated with water vapor variations. A similar but smaller bias is also observed for the low clouds, primarily due to the clear sky effect since the TOA longwave radiation is largely determined by the atmosphere above when the clouds are low-level. Further studies are needed to address this problem. For high clouds, depending on the optical thickness, the model-simulated LW radiances can be either less or greater than the observed ones. When the clouds are very optically thin, the model underestimates the TOA LW radiance as a result of the fact that these clouds tend to be placed too high during the visible adjustment step of ISCCP retrieval. In general, the modeled TOA LW radiances agree better with

observations for the nadir-viewing pixels than for the pixels viewed from limb, since the excessively large limb-viewing pixels are more likely to be heterogeneous or partially cloud-filled.

Compared with the radiative transfer model, the limb-darkening in the ERBE angular models appears to be too weak for the optically thin clouds, but too strong for the optically thick clouds, and the difference between the ERBE ADMs and the angle treatment of the radiative transfer model increases with cloud height. Limitations in the radiative transfer model calculations, however, prevent definitive judgement on the ERBE angular models for the following reasons: 1) The radiative transfer model's angle treatment is sensitive to the uncertainties in the cloud vertical structure (e.g., multi-layer clouds); and 2) the ERBE ADMs are generated using the complete range of observed cloud conditions, not just clear and overcast, whereas the plane-parallel radiative transfer model used in this study inevitably assumes optical homogeneity on the underlying pixels, which tends to underestimate the limb-darkening for the broken three-dimensional cloud fields. Nevertheless, this study clearly demonstrates that obtaining more accurate instantaneous longwave flux estimations from ERBE approach would require additional cloud classes based on cloud height and optical thickness as is planned for the advanced CERES analysis (Wielicki et al. 1996).

One of the rationales behind the ERBE approach is that the viewing-zenith angle dependence of derived longwave flux caused by errors in the angular models will be significantly reduced in the final space- and time-averaged fluxes. This error reduction results from the fact that the ERBE angular models are normalized by the hemispherical flux based on the integral relationship between radiance and flux (Suttles et al., 1989). Over a long enough time periods, a satellite will view a given region of the earth from a wide range of viewing zenith angles, in effect averaging over the viewing zenith angle dependence of the derived longwave fluxes. However, the errors cannot be completely eliminated 1) because of the inability of a satellite platform to provide a uniform sampling in angle (Suttles et al. 1992), 2) because a particular radiometer may only scan over a limited range of viewing zenith angles (for example, the maximum viewing zenith angle of ScaRaB scanning radiometer is 63.57^{o}) or the measurements are not used beyond a cutoff nadir angle since the measurements become increasingly difficult to interpret in terms of the radiant

exitance (Smith et al. 1986), and 3) because the possible convolution between the scene identification and radiance-to-flux conversion steps in the ERBE processing suggests that normalizing the angular model of an individual scene type independently may not be sufficient. Together with the fact that the magnitudes of the errors are cloud type dependent, these residual errors will certainly introduce systematic regional errors in the estimated mean and temporal variations of TOA LW radiation field. For example, as one of the better known interannual variations in climate, ENSO is characterized by large changes in cloud types in consequence of changes in the general circulation pattern of the tropical atmosphere. Unless these systematic, cloud type dependent errors are eliminated, one cannot accurately quantify the spatial and temporal variations in the TOA LW radiative fluxes associated with an ENSO event. Likewise, the ERBE-estimated TOA LW radiative flux gradient across the equatorial Pacific ocean needs to be revisited, considering the persistent and pronounced differences in cloud types over the ascending and descending branches of Walker circulation.

Acknowledgments. We are grateful to Dr. Claudia J. Stubenrauch for the very stimulating discussions on clouds and radiation, and Dr. Yuanchong Zhang for his assistance with the radiative transfer model and for preparing various datasets. This work is supported by the NASA Radiation Sciences Program, previously managed by Dr. Robert Curran and now by Dr. Donald Anderson.

APPENDIX

Error in the visible adjustment step of the ISCCP cloud retrieval

For each cloudy pixel, ISCCP first retrieves the cloud top temperature assuming that the cloud is opaque to infrared radiation, then adjusts the retrieved cloud top temperature and visible optical thickness through iteration if the infrared transmission of the cloud is greater than 0.5% (Rossow et al. 1996). Unfortunately, a small coding error in the ISCCP cloud retrieval program that occasionally causes this iteration to stop prematurely has been found (for the May 1994 ScaRaB DX, this coding error affects about 13% of daytime cloudy pixels). Even though the retrieval program was modified to rectify this error to produce the ScaRaB DX used in this study (as well as for the regular ISCCP data product beyond 1993), we document the error and assess to what extent it affects the retrieved cloud properties and calculated TOA radiative fluxes.

Fig. A1 shows the zonal mean difference between the ScaRaB DX cloud top pressure retrieved using the revised program and the program with the coding error in the visible adjustment step. By presenting the results from different optical thickness intervals separately, it is clear that this error is most noticeable for the cloudy pixels with medium optical thickness values (approximately from 2 to 6) and usually gives rise to a cloud top temperature/pressure value that is a bit too large (about 60 mb in P_c in the worst case). Similar results were also obtained for one month (July 1994) NOAA DX data (not shown). It is also observed that this error decreases as cloud top temperature/pressure increases (not shown). Correction of this error has the effect of moving the cloudy pixels a little bit higher in altitude while also making them slightly optically thinner, resulting in only a very small shift in the relative abundance of the standard ISCCP cloud types. Analysis shows that the small shift occurs mostly from altostratus to cirrus clouds with the changes in either cloud type amounting to less than 1% (absolute value).

Fig. A2 examines the resulting difference in the model calculated TOA LW radiative fluxes using one month (May 1994) ScaRaB DX data (revised minus flawed). This figure shows that the error leads to an overestimation of several Wm^{-2} in the zonal mean TOA LW fluxes for

clouds with medium optical thickness values, consistent with the bias in the retrieved cloud top pressure. When all pixels (cloudy and clear) are included, the global mean TOA LW flux bias owing to this error is only 0.6 Wm^{-2}, indicating that the overall impact of this error on the TOA radiation budget calculation is quite small.

References:

Barkstrom, B. R., and G. L. Smith, 1986: The Earth Radiation Budget Experiment: Science and implementation. *Rev. Geophys.*, **24**, 379-390.

Barkstrom, B. R., E. F. Harrison, G. L. Smith, R. N. Green, J. Kibler, R. Cess, and the ERBE science team, 1989: Earth Radiation Budget Experiment (ERBE) archival and April 1985 results. *Bull. Amer. Meteor. Soc.*, **70,** 1254-1262.

Briand, V., C. J. Stubenrauch, W. B. Rossow, A. Walker, R. Holz, 1998: Scene identification for ScaRaB data: The ISCCP approach. *Satellite Remote Sensing of Clouds and the Atmosphere,* J. D. Haigh, Ed., SPIE, 242-252.

Brooks, D. R., E. H. Harrison, P. Minnis, J. T. Suttles, and R. Kandel, 1986: Development of algorithms for understanding the temporal and spatial variability of the Earth's Radiation Balance. *Rev. Geophys.*, **24,** 422-438.

Capderou, M., 1998: Confirmation of helmholtz reciprocity using ScaRaB satellite data. *Remote Sens. Environ.*, **64,** 266-285.

Chang, F.-L., Z. Li, and S. A. Ackerman, 2000a: Examining the relationship between cloud and radiation quantities derived from satellite observations and model calculations. *J. Climate,* **13,** 3842-3859.

Chang, F.-L., Z. Li, and A. P. Trishchenko, 2000b: The dependence of TOA reflectance anisotropy on cloud properties inferred from ScaRaB satellite data. *J. Appl. Meteor.*, **39,** 2480-2493.

Chen, T., W. B. Rossow, and Y.-C. Zhang, 2000a: Radiative effects of cloud-type variations. *J. Climate,* **13,** 264-286.

Chen, T., Y.-C. Zhang, and W. B. Rossow, 2000b: Sensitivity of atmospheric radiative heating rate profiles to variations of cloud layer overlap. *J. Climate,* **13,** 2941-2959.

Collins, W. D., and A. K. Inamdar, 1995: Validation of clear-sky fluxes for tropical oceans from the Earth Radiation Budget Experiment. *J. Climate,* **8,** 569-578.

Diekmann, F. J., and G. L. Smith, 1989: Investigation of scene identification algorithms for radiation budget measurements. *J. Geophys. Res.,* **94,** 3395-3412.

Gruber, A., and A. F. Krueger, 1984: The status of the NOAA outgoing longwave radiation data set. *Bull. Amer. Meteor. Soc.,* **65,** 958-962.

Gruber, A., R. Ellingson, P. Ardanuy, M. Weiss, S. K. Yang, and S. N. Oh, 1994: A comparison of ERBE and AVHRR longwave flux estimates. *Bull. Amer. Meteor. Soc.,* **75,** 2115-2130.

Harrison, E. F., P. Minnis, B. R. Barkstrom, V. Ramanathan, R. D. Cess, and G. G. Gibson, 1990: Seasonal variation of cloud radiative forcing derived from the Earth Radiation Budget Experiment. *J. Geophys. Res.,* **95,** 18 687-18 703.

Hartmann, D. L., and D. Doelling, 1991: On the net radiative effectiveness of clouds. *J. Geophys. Res.,* **96,** 869-891.

Hartmann, D. L., M. E. Ockert-Bell, and M. L. Michelsen, 1992: The effect of cloud type on Earth's energy balance: Global analysis. *J. Climate,* **5,** 1281-1304.

Hatzianastassiou, N., and I. Vardavas, 1999: The net radiation budget of the Northern Hemisphere. *J. Geophys. Res.*, **104,** 27341-27359.

Jacobowitz, H., H. V. Soule, H. L. Kyle, F. B. House, and the Nimbus 7 ERB Experiment Team, 1984: The earth radiation budget (ERB) experiment: An overview. *J. Geophys. Res.*, **89,** 5021-5038.

Kandel, R. S., J.-L. Monge, M. Viollier, L. A. Pakhomov, V. I. Adasko, R. G. Reitenbach, E. Raschke, and R. Stuhlmann, 1994: The ScaRaB project: Earth radiation budget observations from the Meteor satellites. World Space Congress (Washington 1992)_COSPAR Symp. A.2-S. *Adv. Space Res.*, **14(1),** 47-54.

Kandel, R., M. Viollier, P. Raberanto, J. Ph. Duvel, L. A. Pakhomov, V. A. Golovko, A. P. Trishchenko, J. Mueller, E. Raschke, R. Stuhlmann, and the International ScaRaB Scientific Working Group (ISSWG), 1998: The ScaRaB earth radiation budget dataset. *Bull. Amer. Meteor. Soc.*, **79,** 765-783.

Kidwell, K. B., 1995: NOAA Polar Orbiter Data Users Guide (TIROS-N, NOAA-6, NOAA-7, NOAA-8, NOAA-9, NOAA-10, NOAA-11, NOAA-12, NOAA-13 and NOAA-14). National Environmental Satellite, Data and Information Service, Washington, DC, 394 pp.

Lacis, A. A., and V. Oinas, 1991: A description of the correlated k-distribution method for modeling non-grey gaseous absorption, thermal emission, and multiple scattering on vertically inhomogeneous atmospheres. *J. Geophys. Res.*, **96,** 9027-9063.

Lau, N.-C., and M. W. Crane, 1995: A satellite view of the synoptic-scale organization of cloud properties in midlatitude and tropical circulation systems. *Mon. Wea. Rev.*, **123,** 1984-2006.

Ma, Q., and R.H. Tipping, 1991: A far wing line shape theory and its application to the water vapor continuum absorption in the infrared region, I. *J. Chem. Phys.*, **95,** 6290-6301.

Ma, Q., and R.H. Tipping, 1992a: A far wing line shape theory and its application to the water vibrational bands, II. *J. Chem. Phys.*, **96,** 8655-8663.

Ma, Q., and R.H. Tipping, 1992b: A far wing line shape theory and its application to the foreign-broadened water continuum absorption, III. *J. Chem. Phys.*, **97,** 818-828.

Ockert-Bell, M. E., and D. L. Hartmann, 1992: The effect of cloud type on earth's energy balance: Results for selected regions. *J. Climate,* **5,** 1158-1171.

Ohring, G., A. Gruber, and R. Ellingson, 1984: Satellite determinations of the relationship between total longwave radiation flux and infrared window radiance. *J. Clim. Appl. Meteor.,* **23,** 416-425.

Rossow, W. B., and L. C. Garder, 1993a: Cloud detection using satellite measurements of infrared and visible radiances for ISCCP. *J. Climate,* **6,** 2341-2369.

Rossow, W. B., and L. C. Garder, 1993b: Validation of ISCCP cloud detections. *J. Climate,* **6,** 2370-2393.

Rossow, W. B., and A. A. Lacis, 1990: Global, seasonal cloud variations from satellite radiance measurements. Part II: Cloud properties and radiative effects. *J. Climate,* **3,** 1204-1253.

Rossow, W. B., and R. A. Schiffer, 1991: ISCCP cloud data products. *Bull. Amer. Meteor. Soc.,* **72,** 2-20.

Rossow, W. B., and R. A. Schiffer, 1999: Advances in understanding clouds from ISCCP. *Bull. Amer. Meteor. Soc.*, **80**, 2261-2288.

Rossow, W. B., and Y.-C. Zhang, 1995: Calculation of surface and top of atmosphere radiative fluxes from physical quantities based on ISCCP datasets, 2: Validation and first results, *J. Geophys. Res.*, **100,** 1167-1197.

Rossow, W. B., A. W. Walker, and L. C. Garder, 1993: Comparison of ISCCP and other cloud amounts. *J. Climate,* **6,** 2394-2418.

Rossow, W. B., A. W. Walker, D. E. Beuschel, and M. D. Roiter, 1996: International Satellite Cloud Climatology Project (ISCCP) Documentation of New Cloud Datasets. Tech. Doc. WMO/TD 737, World Climate Research Programme, Geneva, Switzerland, 115 pp.

Schiffer, R. A., and W. B. Rossow, 1983: The International Satellite Cloud Climatology Project (ISCCP): The first project of the World Climate Research Program. *Bull. Amer. Meteor. Soc.,* **64,** 779-784.

Scott, N. A., A. Chédin, R. Armante, J. Francis, C. Stubenrauch, J.-P. Chaboureau, F. Chevallier, C. Claud, F. Cheruy, 1999: Characteristics of the TOVS Pathfinder Path-B Dataset. *Bull. Amer. Meteor. Soc.,* **80,** 2679-2702.

Smith, G. L., R. N. Green, E. Raschke, L. M. Avis, J. T. Suttles, B. A. Wielicki, and R. Davies, 1986: Inversion methods for satellite studies of the earth's radiation budget: Development of algorithms for the ERBE mission. *Rev. Geophys.*, **24,** 407-421.

Stowe, L. L., C. G. Wellemeyer, T. F. Eck, H. Y. M. Yeh, and the Nimbus-7 Cloud Data Processing Team, 1988: Nimbus-7 global cloud climatology. Part I: Algorithms and validation. *J. Climate,* **1,** 445-470.

Stubenrauch, C., J.-P. Duvel, and R. S. Kandel, 1993: Determination of longwave anisotropic emission factors from combined broad- and narrowband radiance measurements. *J. Appl. Meteor.,* **32,** 848-856.

Suttles, J. T., R. N. Green, P. Minnis, G. L. Smith, W. F. Staylor, B. A. Wielicki, I. J. Walker, D. F. Young, V. R. Taylor, and L. L. Stowe, 1988: *Angular Radiation Models for Earth-Atmosphere System, Volume I: Shortwave Radiation.* NASA Ref. Pub. RP 1184 vol. I, Langley Research Center, Hampton, Virginia, 144 pp.

Suttles, J. T., R. N. Green, G. L. Smith, B. A. Wielicki, I. J. Walker, V. R. Taylor, and L. L. Stowe, 1989: *Angular Radiation Models for Earth-Atmosphere System, Volume II: Longwave Radiation.* NASA Ref. Pub. RP 1184 vol. II, Langley Research Center, Hampton, Virginia, 84 pp.

Suttles, J. T., B. A. Wielicki, and S. Vemury, 1992: Top-of-atmosphere radiative fluxes: Validation of ERBE scanner inversion algorithm using *Nimbus-7* ERB data. *J. Appl. Meteorol.,* **31,** 784-796.

Viollier M., R. Kandel, and P. Raberanto, 1995: Inversion and space-time-averaging algorithms for ScaRaB (Scanner for the Earth Radiation Budget)—Comparison with ERBE. *Ann. Geophys.,* **13,** 959-968.

Wielicki, B. A. and R. N. Green, 1989: Cloud identification for ERBE radiative flux retrieval. *J. Appl. Meteor.,* **28,** 1133-1146.

Wielicki, B. A., B. R. Barkstrom, E. F. Harrison, R. B. Lee III, G. L. Smith, and J. E. Cooper, 1996: Clouds and the Earth's Radiant Energy System (CERES): An Earth Observing System Experiment. *Bull. Amer. Meteor. Soc.*, **77,** 853-868.

Xu, F., 1997: Outgoing Longwave Radiation (OLR): Variability and Retrieval. Ph.D. dissertation, Columbia University, 173 pp.

Ye, Q., and J. A. Coakley Jr., 1996a: Biases in Earth radiation budget observations, 1, Effects of scanner spatial resolution on the observed anisotropy. *J. Geophys. Res.*, **101,** 21243-21252.

Ye, Q., and J. A. Coakley Jr., 1996b: Biases in Earth radiation budget observations. 2. Consistent scene identification and anisotropic factors. *J. Geophys. Res.*, **101,** 21253-21263.

Zhang, Y.-C., W. B. Rossow, and A. A. Lacis, 1995: Calculation of the surface and top of atmosphere radiative fluxes from physical quantities based on ISCCP data set, 1: Method and sensitivity to input data uncertainties. *J. Geophys. Res.*, **100,** 1149-1165.

Table captions:

Table 1. Distribution of the ISCCP-derived scene types in each of the MLE-derived cloud cover categories, as well as the frequency of occurrence of each ISCCP-derived scene type for all the ScaRaB pixels spanning May 1994. The highest values are shown in bold.

Table 2. Distribution of the MLE-derived cloud cover categories in each of the ISCCP-derived scene types, as well as the frequency of occurrence of each MLE-derived cloud cover category for all the ScaRaB pixels spanning May 1994. The highest values are shown in bold.

Figure captions:

Figure 1. Schematic diagram of the basic approach used in the present study.

Figure 2. Definitions of the nine different cloud types by ISCCP in terms of cloud-top pressure and visible optical thickness. The names used for convenience are meant to suggest qualitative relationships with the classic morphological cloud types, but they should not be interpreted to be quantitatively correct in every instance (cf. Lau and Crane 1995).

Figure 3. Variation of MLE-derived cloud cover category (c: clear; p: partly cloudy; m: mostly cloudy; o: overcast) frequency of occurrence (FOC) as a function of viewing zenith angle for each of the nine ISCCP-derived cloud types, clear pixels, all cloudy pixels, and all pixels (data month: May 1994)

Figure 4a. Mean differences (over ocean, "unmixed" pixels only) between the measured and model-simulated TOA LW radiances (in $Wm^{-2}sr^{-1}$), between the converted TOA LW fluxes using measured LW radiances (both the results from ERBE ADMs and from SDK ADMs are presented) and model calculated ones (in Wm^{-2}), both for the nadir-viewing pixels (VZA = 0^{o}) and pixels with VZA = 60^{o}. Solid triangles denote the results for clear pixels (data month: May 1994).

Figure 4b. Same as Fig. 4a, but for July 1994.

Figure 5a. Same as Fig. 4a, but only for the pixels where model-simulated and observed TOA LW radiances agree to with 0.5 $Wm^{-2}sr^{-1}$ (data month: May 1994).

Figure 5b. Same as Fig. 5a, but for July 1994.

Figure 6. Scatter plot of TOA LW radiance differences (in $Wm^{-2}sr^{-1}$; observation minus calculation, nadir-viewing pixels only) against the column precipitable water using (a) TOVS, (b) 3I atmospheric temperature and humidity profile, along with the corresponding correlation coefficient (data month: May 1994).

Figure 7. Mean and standard deviation of TOA LW radiance differences (in $Wm^{-2}sr^{-1}$; observation minus calculation) as a function of σ_{Tc} (the standard deviation of cloud top temperatures over the 16 neighboring ISCCP DX pixels; in K) for the 60° view, ocean ScaRaB pixels classified as high-level clouds with optical thickness larger than 1 by ISCCP (data month: May 1994).

Figure 8. Same as Fig. 4a, but for the "mixed" pixels only.

Figure 9. Same as Fig. 5a, but for the "mixed" pixels only.

Figure A1. Zonal mean difference between the ScaRaB DX cloud top pressure retrieved using the revised ISCCP cloud program and the program with a coding error in the visible adjustment step for May (top panel) and July (bottom panel) 1994.

Figure A2. Zonal mean difference in the model calculated TOA LW radiative fluxes (in Wm^{-2}) using May 1994 ScaRaB DX data (revised minus flawed).

ISCCP Scene Type		ERBE MLE Scene Type			
		Clear (Clr)	Partly Cloudy (Pc)	Mostly Cloudy (Mc)	Overcast (Oc)
37.1%	Clear (Clr)	**58.4%**	29.6%	4.4%	7.6%
13.1%	Cumulus (Cu)	8.6%	**74.3%**	14.0%	3.1%
15.2%	Stratocumulus (Sc)	7.7%	23.1%	**63.5%**	5.7%
1.6%	Stratus (St)	24.6%	0%	**38.1%**	37.3%
9.5%	Altocumulus (Ac)	5.9%	27.6%	**47.7%**	18.8%
7.4%	Altostratus (As)	7.6%	1.2%	**50.8%**	40.4%
1.4%	Nimbostratus (Ns)	20.9%	0%	9.1%	**70.0%**
8.1%	Cirrus (Ci)	11.3%	22.2%	32.9%	**33.6%**
4.9%	Cirrostratus (Cs)	0%	0%	2.8%	**97.2%**
1.7%	Deep Convective (Dc)	0.5%	0%	0%	**99.5%**
62.9%	Cloudy	8.0%	27.9%	**36.9%**	27.2%

Table 1

ERBE MLE Scene Type		ISCCP Scene Type									
		Clr	Cu	Sc	St	Ac	As	Ns	Ci	Cs	Dc
26.3%	Clr	**80.7%**	4.3%	4.4%	1.4%	2.2%	2.2%	1.2%	3.6%	0%	0%
28.5%	Pc	**37.6%**	34.0%	12.2%	0%	9.4%	0.3%	0%	6.5%	0%	0%
25.1%	Mc	6.3%	7.3%	**38.2%**	2.3%	18.4%	15.5%	0.5%	10.9%	0.6%	0%
20.1%	Oc	13.8%	2.0%	4.3%	2.8%	9.0%	15.4%	5.1%	14.0%	**24.7%**	8.8%

Table 2

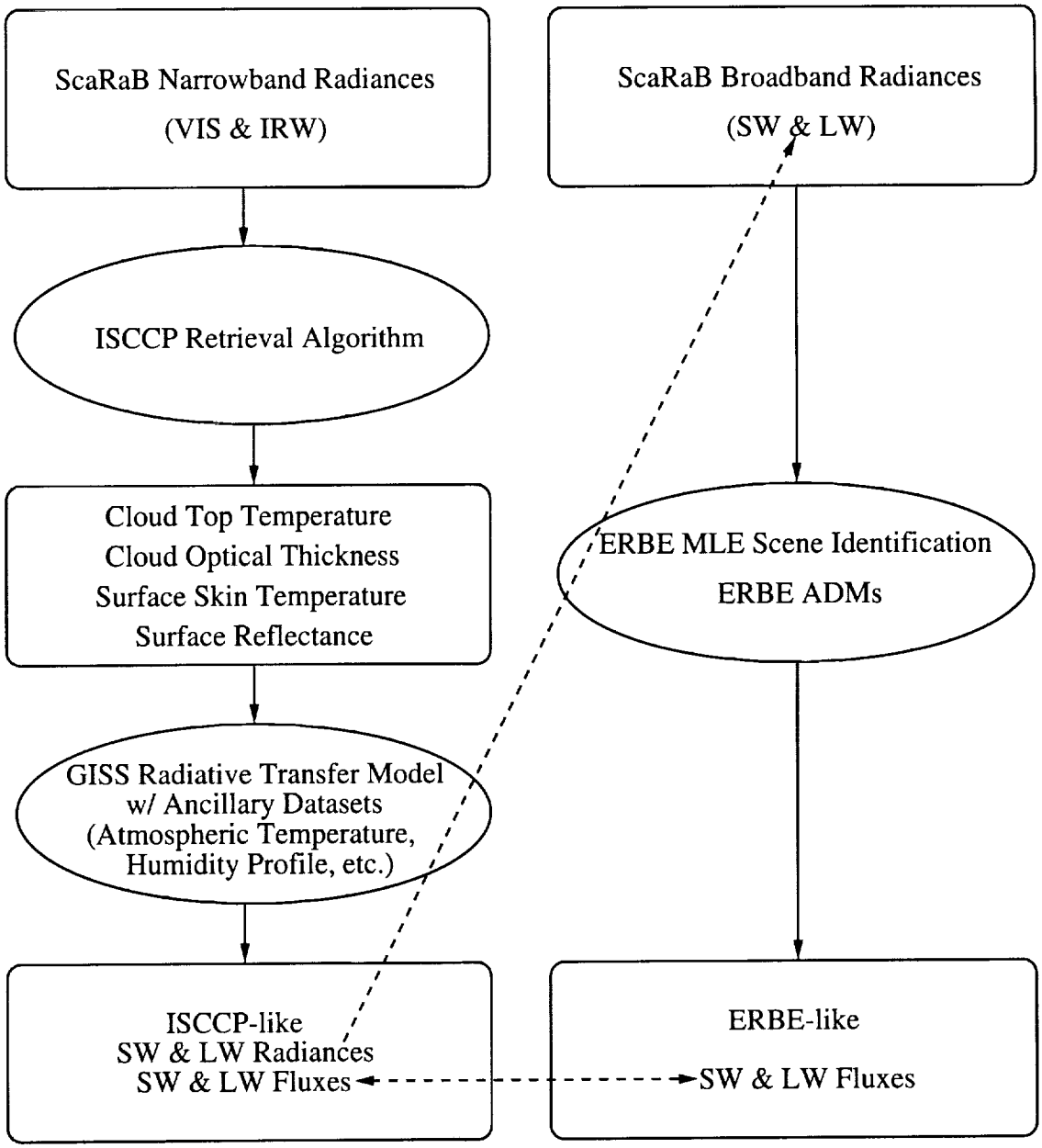
ScaRaB Narrowband Radiances
(VIS & IRW)
ScaRaB Broadband Radiances
(SW & LW)
ISCCP Retrieval Algorithm
Cloud Top Temperature
Cloud Optical Thickness
Surface Skin Temperature
Surface Reflectance
ERBE MLE Scene Identification
ERBE ADMs
GISS Radiative Transfer Model
w/ Ancillary Datasets
(Atmospheric Temperature,
Humidity Profile, etc.)
ISCCP-like
SW & LW Radiances
SW & LW Fluxes
ERBE-like
SW & LW Fluxes

Fig. 1

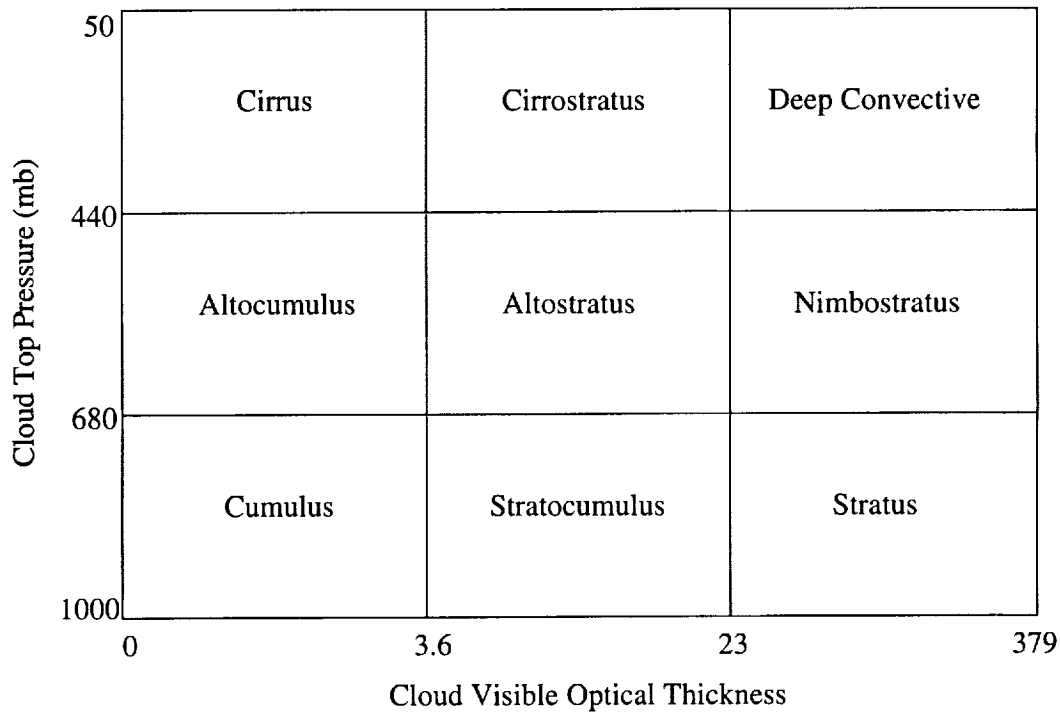
Cirrus
Cirrostratus
Deep Convective
Altocumulus
Altostratus
Nimbostratus
Cumulus
Stratocumulus
Stratus
50
440
680
1000
0
3.6
23
379
Cloud Top Pressure (mb)
Cloud Visible Optical Thickness

Fig. 2

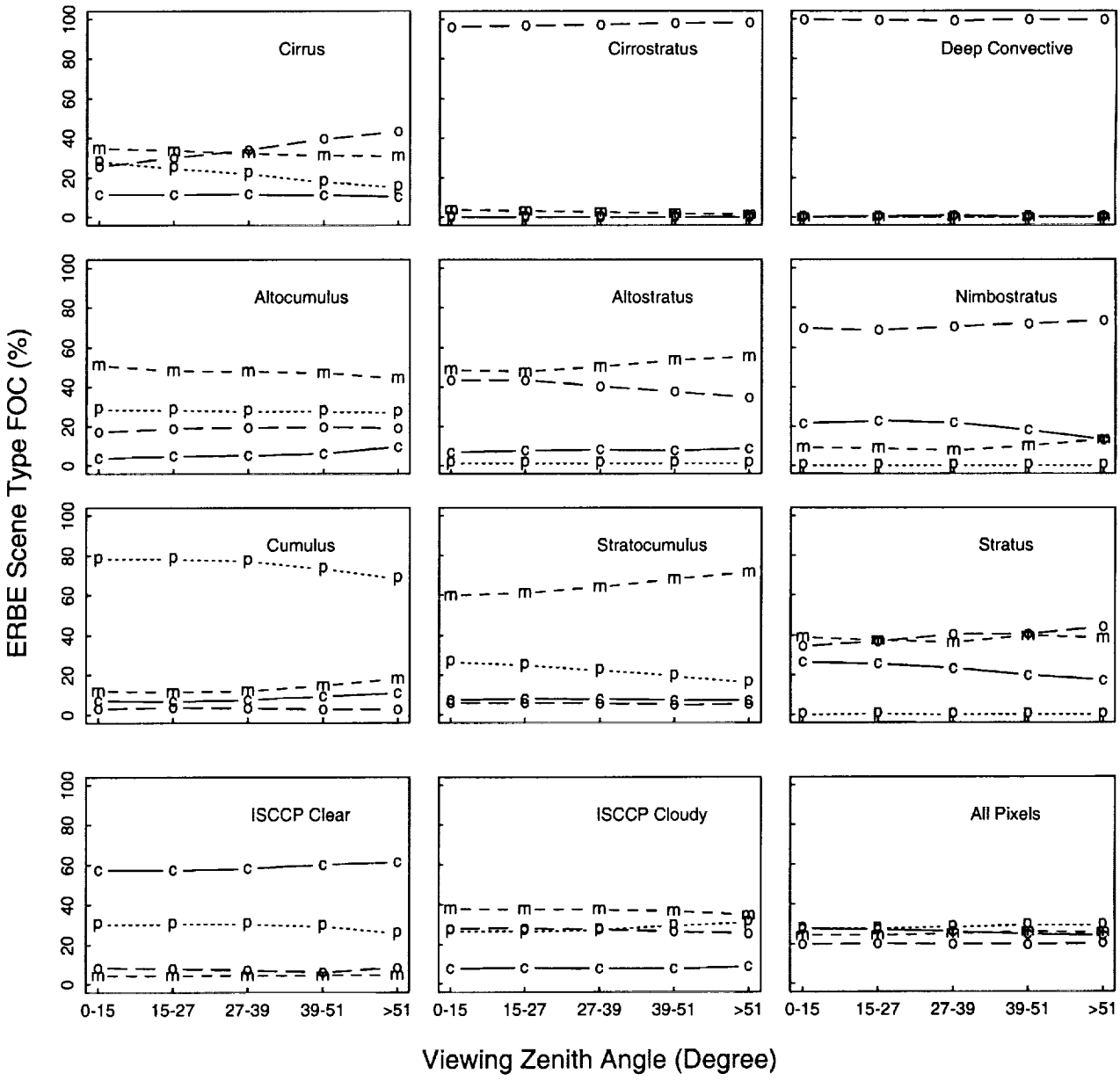
Cirrus
Cirrostratus
Deep Convective
Altocumulus
Altostratus
Nimbostratus
Cumulus
Stratocumulus
Stratus
ISCCP Clear
ISCCP Cloudy
All Pixels
ERBE Scene Type FOC (%)
0
20
40
60
80
100
0-15
15-27
27-39
39-51
>51
Viewing Zenith Angle (Degree)

Fig. 3

Ocean

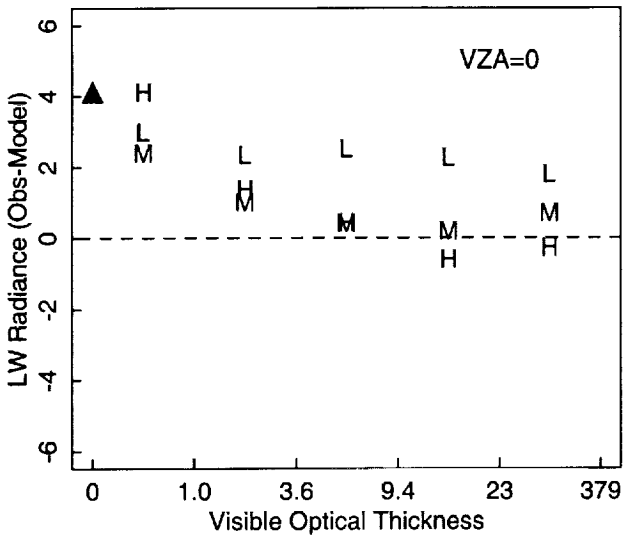
VZA=0
LW Radiance (Obs-Model)
6
4
2
0
-2
-4
-6
0
1.0
3.6
9.4
23
379
Visible Optical Thickness

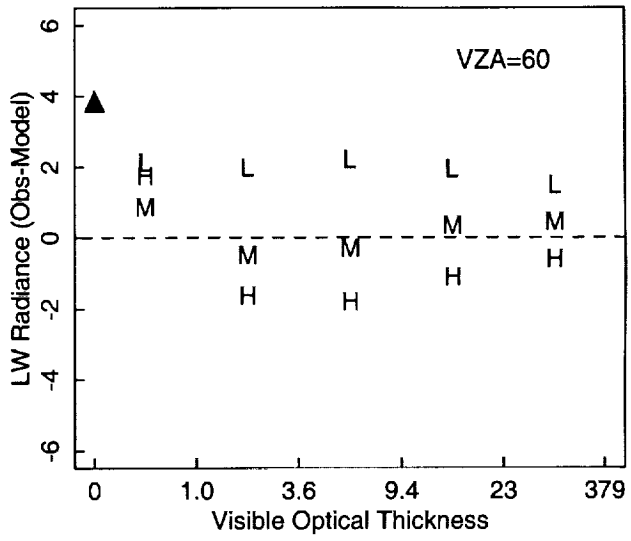
VZA=60
LW Radiance (Obs-Model)
6
4
2
0
-2
-4
-6
0
1.0
3.6
9.4
23
379
Visible Optical Thickness

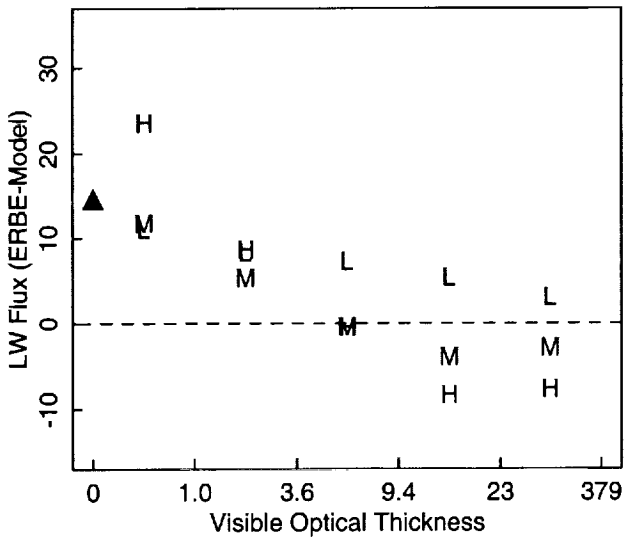
LW Flux (ERBE-Model)
30
20
10
0
-10
0
1.0
3.6
9.4
23
379
Visible Optical Thickness

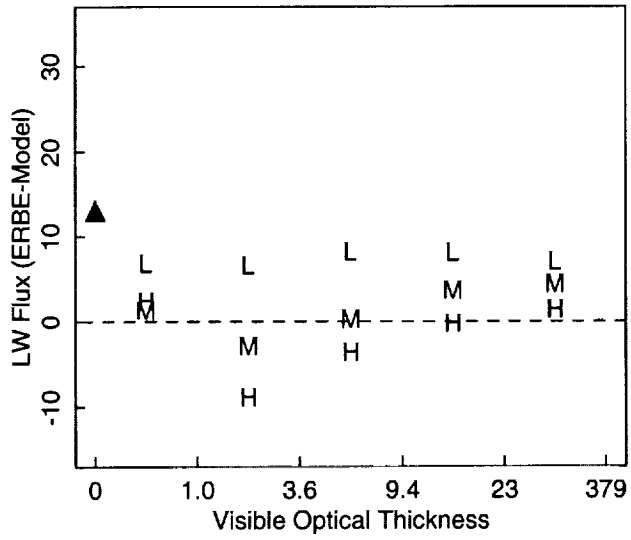
LW Flux (ERBE-Model)
30
20
10
0
-10
0
1.0
3.6
9.4
23
379
Visible Optical Thickness

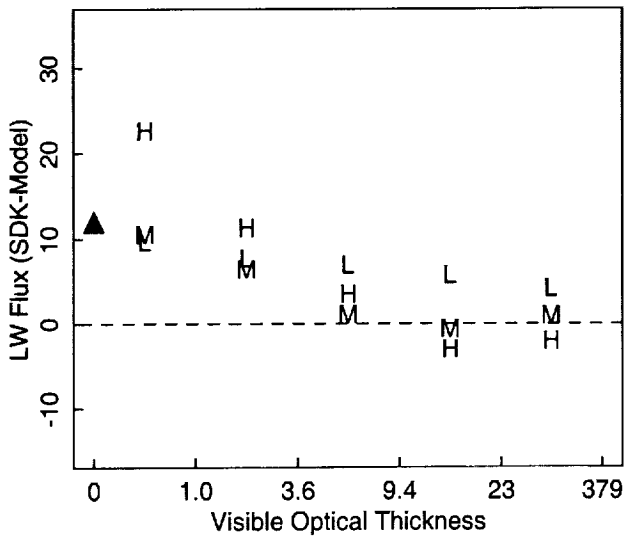
LW Flux (SDK-Model)
30
20
10
0
-10
0
1.0
3.6
9.4
23
379
Visible Optical Thickness

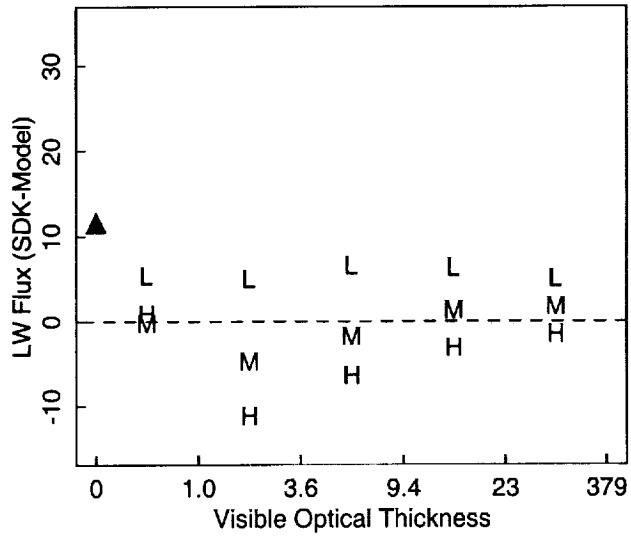
LW Flux (SDK-Model)
30
20
10
0
-10
0
1.0
3.6
9.4
23
379
Visible Optical Thickness

Fig. 4a

Ocean

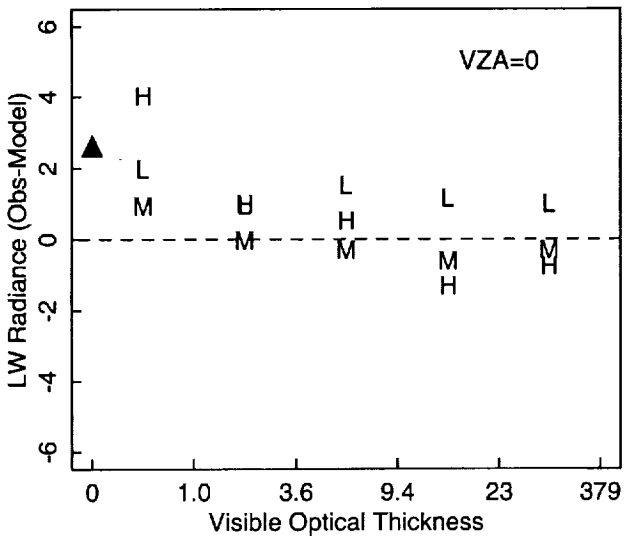
VZA=0
LW Radiance (Obs-Model)
6
4
2
0
-2
-4
-6
0
1.0
3.6
9.4
23
379
Visible Optical Thickness

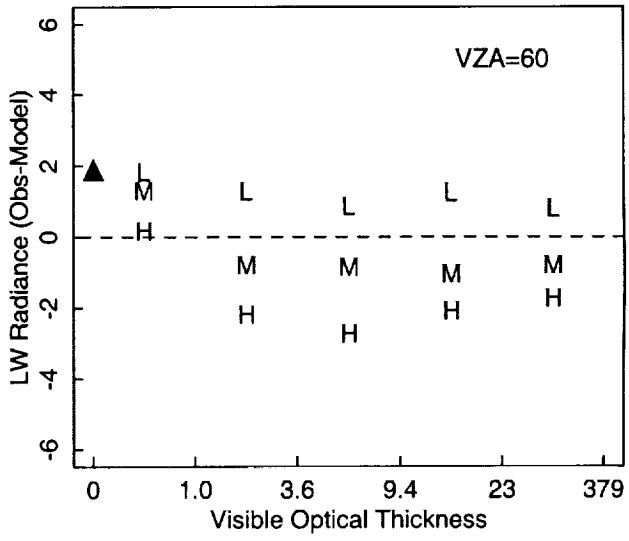
VZA=60
LW Radiance (Obs-Model)
6
4
2
0
-2
-4
-6
0
1.0
3.6
9.4
23
379
Visible Optical Thickness

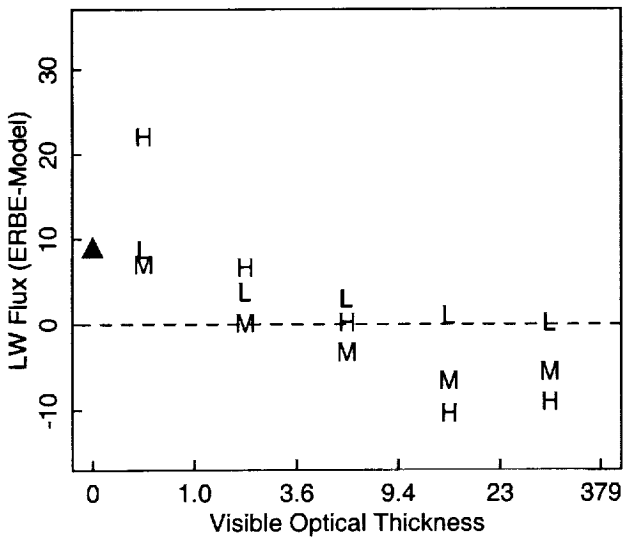
LW Flux (ERBE-Model)
30
20
10
0
-10
0
1.0
3.6
9.4
23
379
Visible Optical Thickness

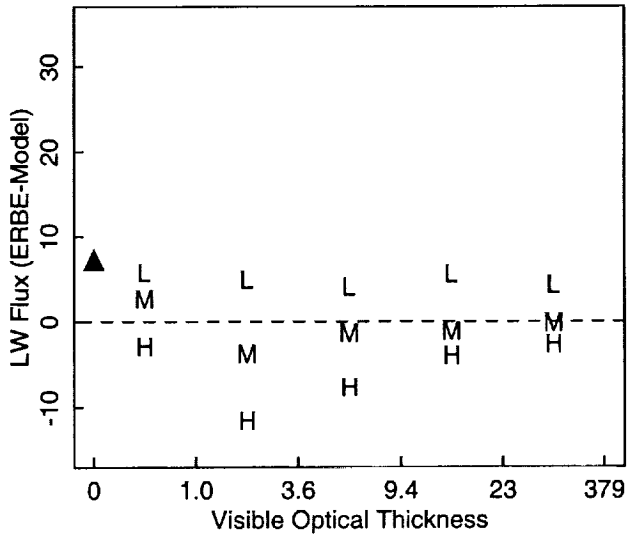
LW Flux (ERBE-Model)
30
20
10
0
-10
0
1.0
3.6
9.4
23
379
Visible Optical Thickness

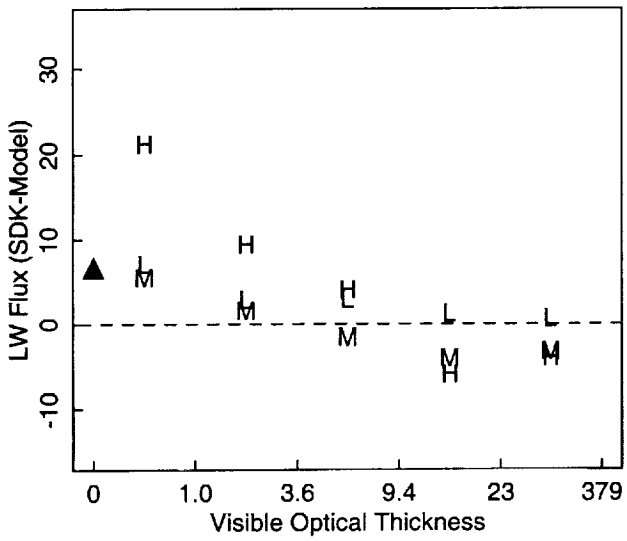
LW Flux (SDK-Model)
30
20
10
0
-10
0
1.0
3.6
9.4
23
379
Visible Optical Thickness

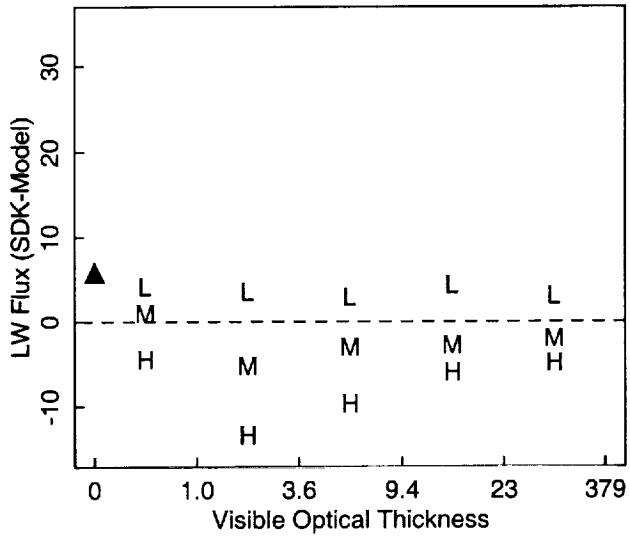
LW Flux (SDK-Model)
30
20
10
0
-10
0
1.0
3.6
9.4
23
379
Visible Optical Thickness

Fig. 4b

Ocean

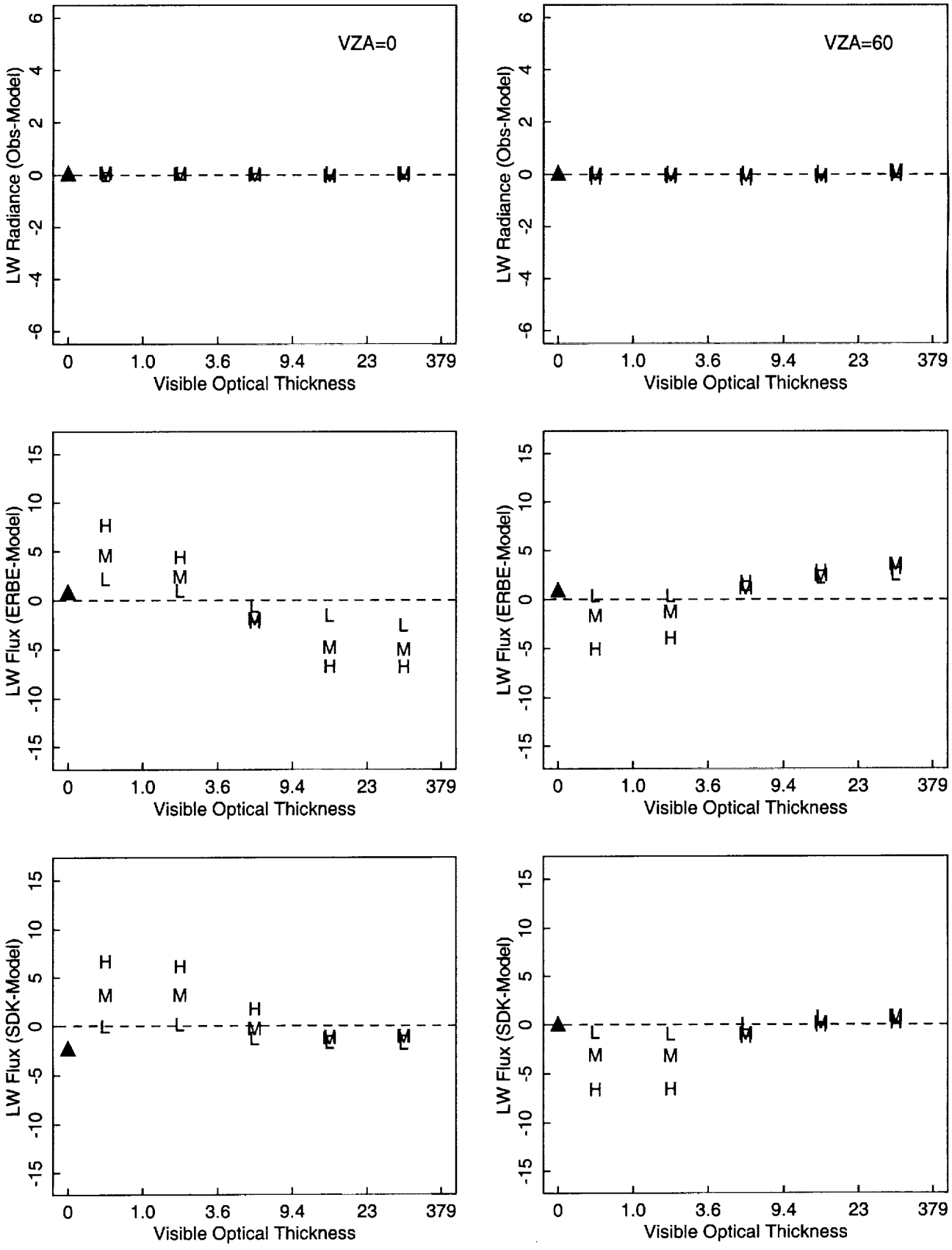
VZA=0
VZA=60
LW Radiance (Obs-Model)
LW Flux (ERBE-Model)
LW Flux (SDK-Model)
Visible Optical Thickness
0
1.0
3.6
9.4
23
379
-6
-4
-2
0
2
4
6
-15
-10
-5
0
5
10
15
H
M
L

Fig. 5a

Ocean

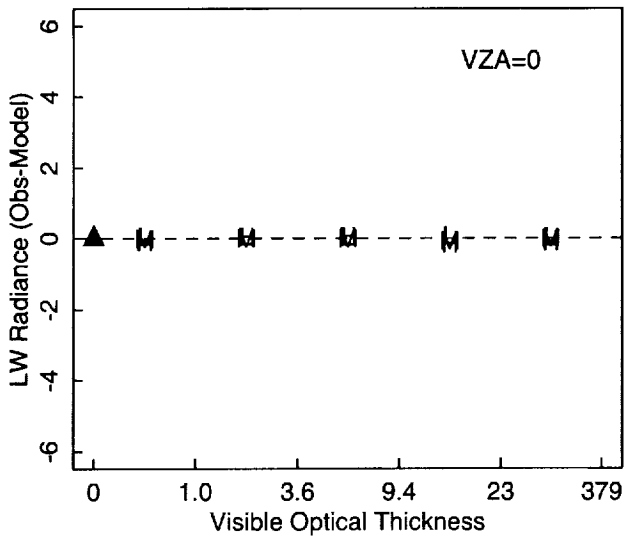
VZA=0
LW Radiance (Obs-Model)
6
4
2
0
-2
-4
-6
0
1.0
3.6
9.4
23
379
Visible Optical Thickness

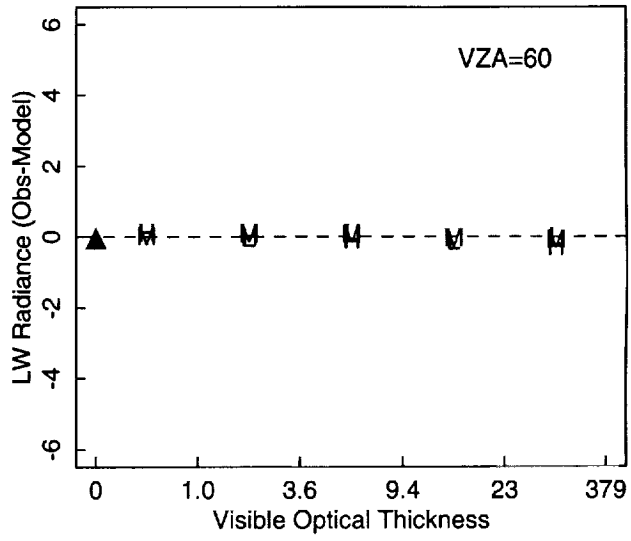
VZA=60
LW Radiance (Obs-Model)
6
4
2
0
-2
-4
-6
0
1.0
3.6
9.4
23
379
Visible Optical Thickness

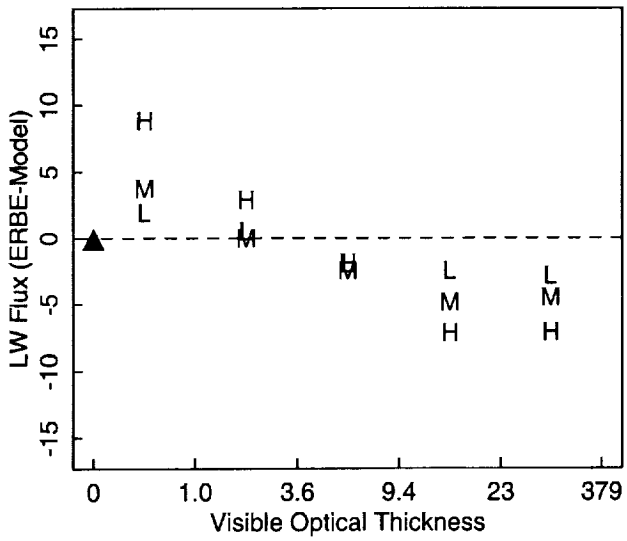
LW Flux (ERBE-Model)
15
10
5
0
-5
-10
-15
0
1.0
3.6
9.4
23
379
Visible Optical Thickness

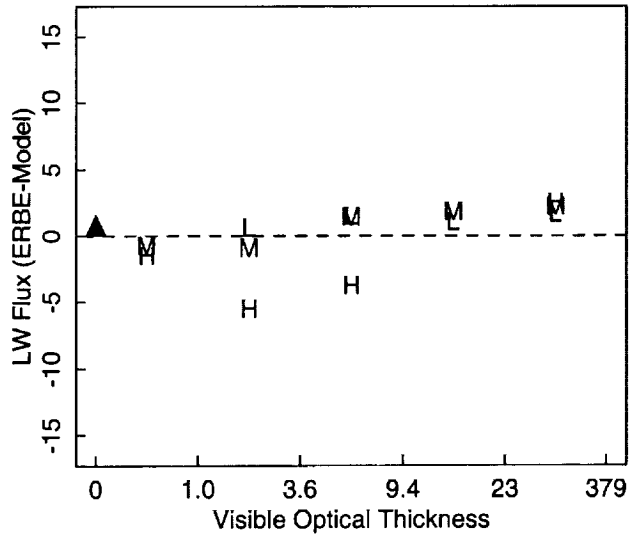
LW Flux (ERBE-Model)
15
10
5
0
-5
-10
-15
0
1.0
3.6
9.4
23
379
Visible Optical Thickness

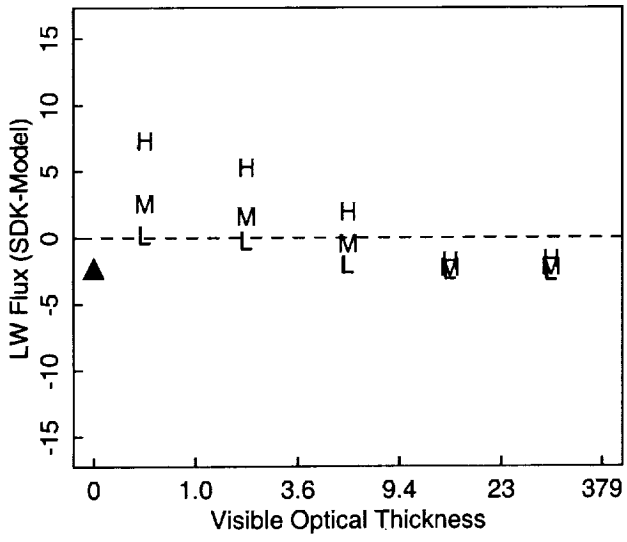
LW Flux (SDK-Model)
15
10
5
0
-5
-10
-15
0
1.0
3.6
9.4
23
379
Visible Optical Thickness

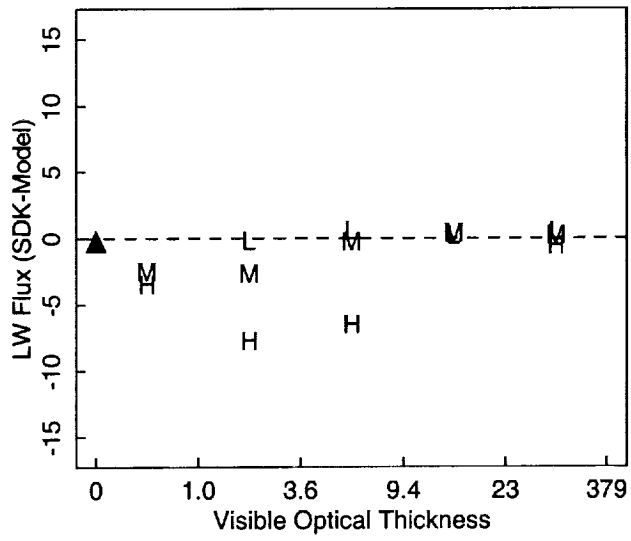
LW Flux (SDK-Model)
15
10
5
0
-5
-10
-15
0
1.0
3.6
9.4
23
379
Visible Optical Thickness

Fig. 5b

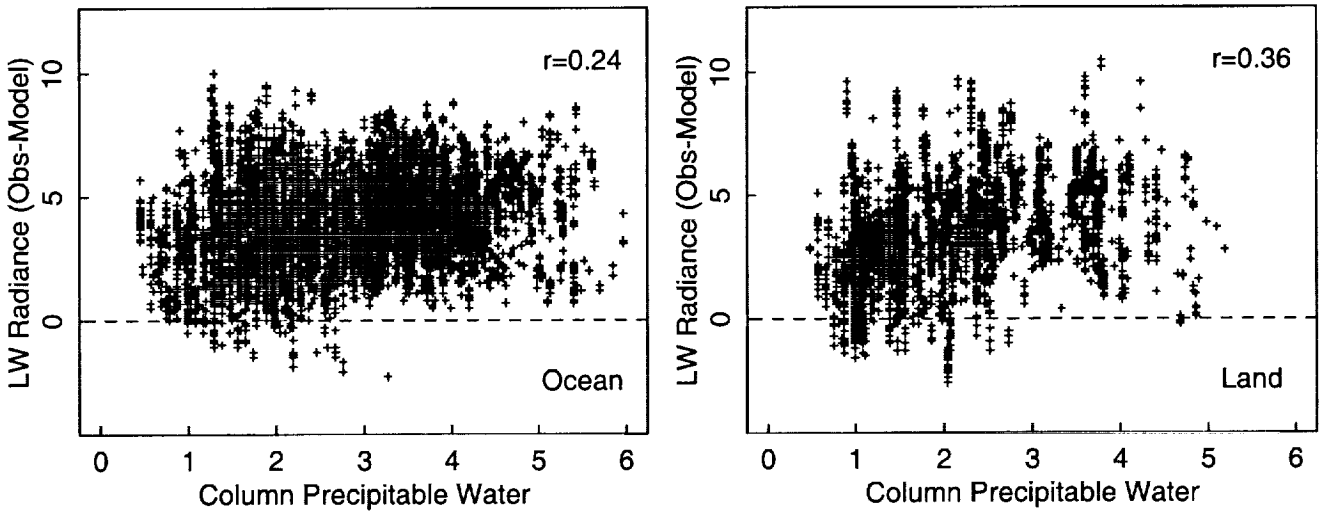
r=0.24
Ocean
LW Radiance (Obs-Model)
Column Precipitable Water
r=0.36
Land
LW Radiance (Obs-Model)
Column Precipitable Water

Fig. 6a

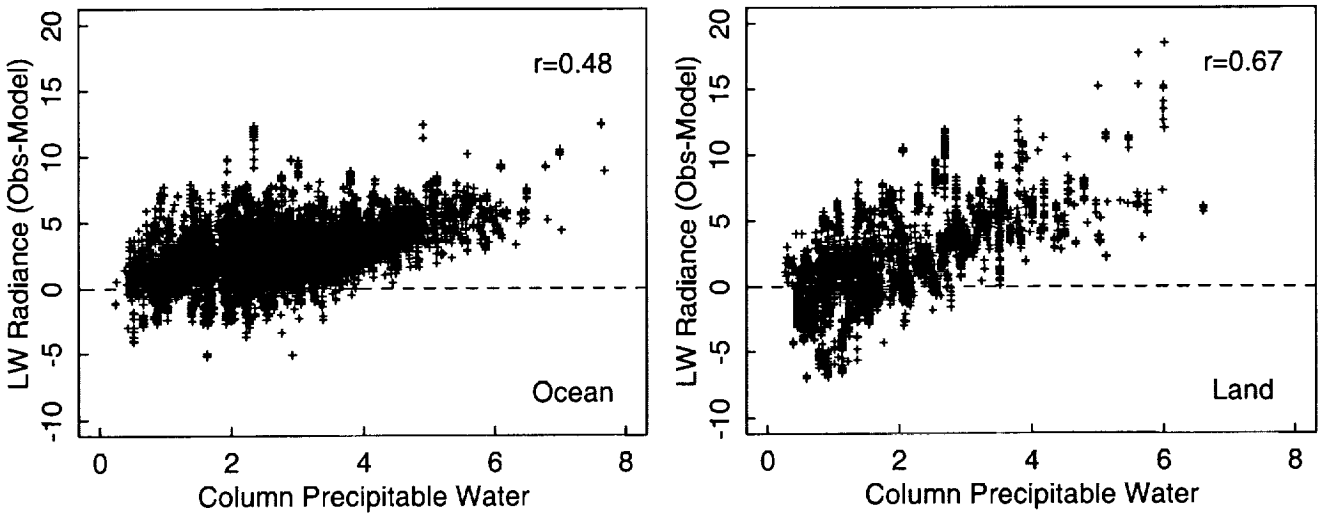
LW Radiance (Obs-Model)
-10
-5
0
5
10
15
20
r=0.48
Ocean
0
2
4
6
8
Column Precipitable Water
LW Radiance (Obs-Model)
-10
-5
0
5
10
15
20
r=0.67
Land
0
2
4
6
8
Column Precipitable Water

Fig. 6b

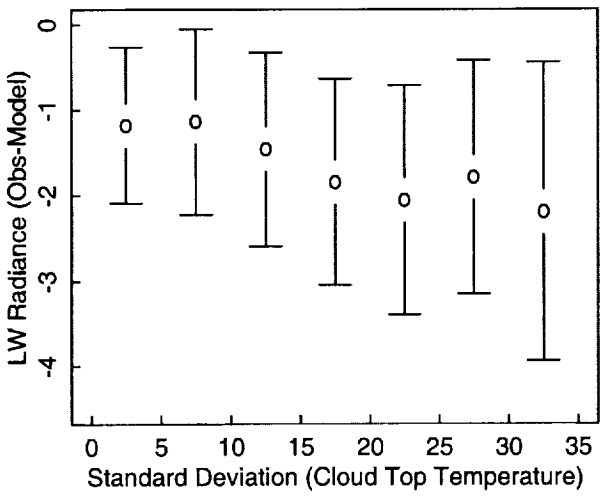
LW Radiance (Obs-Model)
0
-1
-2
-3
-4
0
5
10
15
20
25
30
35
Standard Deviation (Cloud Top Temperature)

Fig. 7

Ocean

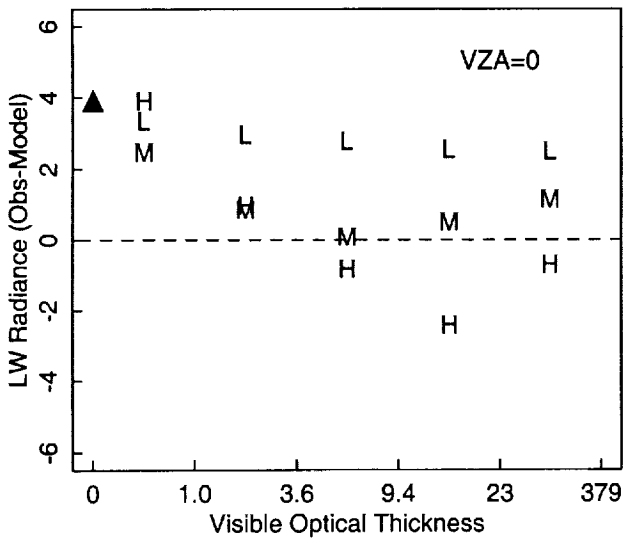
VZA=0
LW Radiance (Obs-Model)
6
4
2
0
-2
-4
-6
0
1.0
3.6
9.4
23
379
Visible Optical Thickness

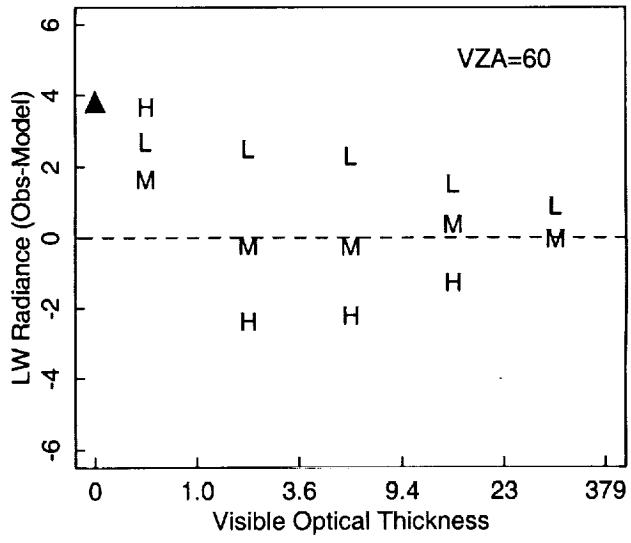
VZA=60
LW Radiance (Obs-Model)
6
4
2
0
-2
-4
-6
0
1.0
3.6
9.4
23
379
Visible Optical Thickness

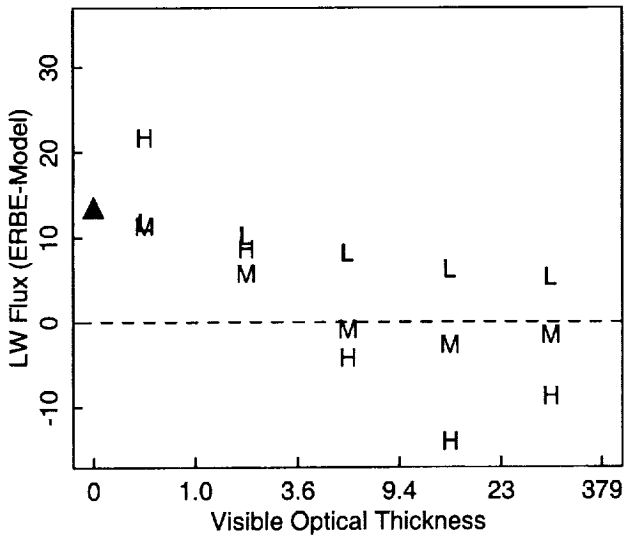
LW Flux (ERBE-Model)
30
20
10
0
-10
0
1.0
3.6
9.4
23
379
Visible Optical Thickness

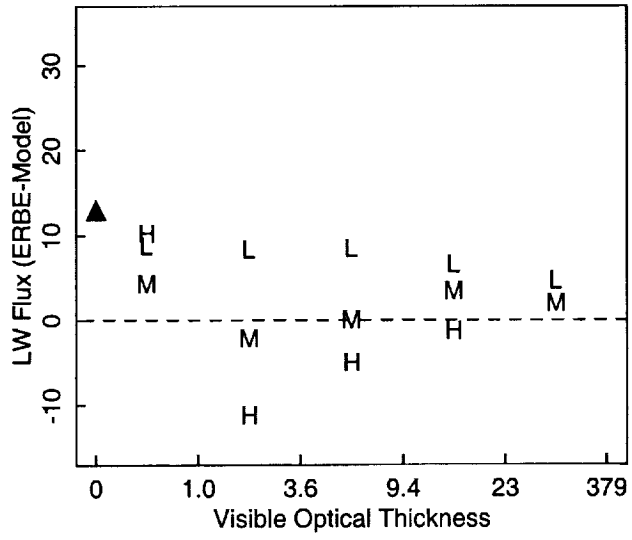
LW Flux (ERBE-Model)
30
20
10
0
-10
0
1.0
3.6
9.4
23
379
Visible Optical Thickness

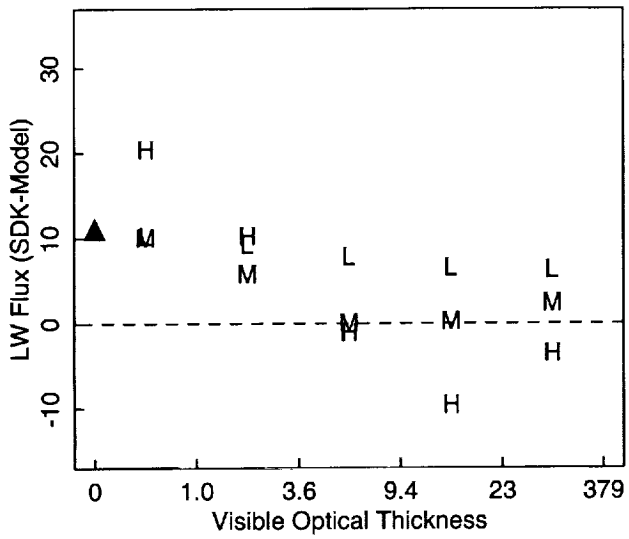
LW Flux (SDK-Model)
30
20
10
0
-10
0
1.0
3.6
9.4
23
379
Visible Optical Thickness

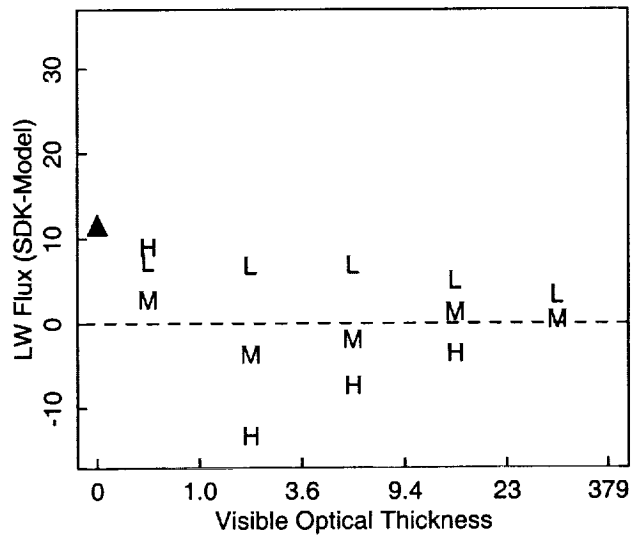
LW Flux (SDK-Model)
30
20
10
0
-10
0
1.0
3.6
9.4
23
379
Visible Optical Thickness

Fig. 8

Ocean

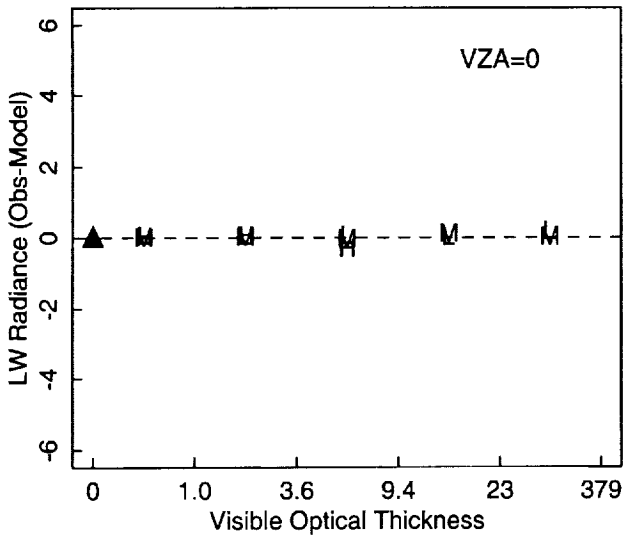
VZA=0
LW Radiance (Obs-Model)
6
4
2
0
-2
-4
-6
0
1.0
3.6
9.4
23
379
Visible Optical Thickness

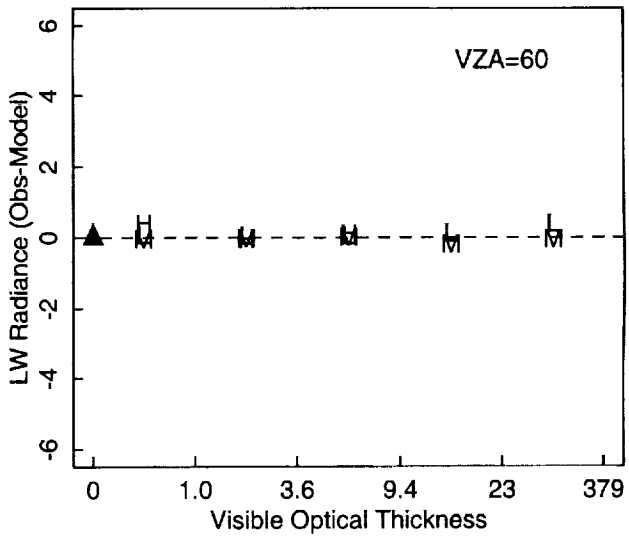
VZA=60
LW Radiance (Obs-Model)
6
4
2
0
-2
-4
-6
0
1.0
3.6
9.4
23
379
Visible Optical Thickness

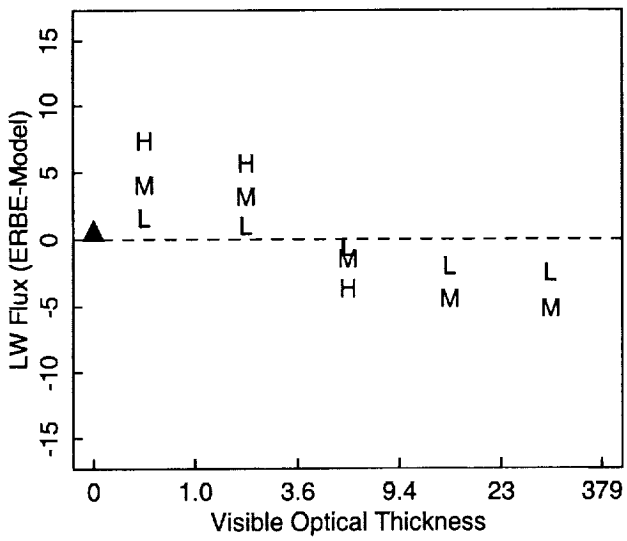
LW Flux (ERBE-Model)
15
10
5
0
-5
-10
-15
0
1.0
3.6
9.4
23
379
Visible Optical Thickness

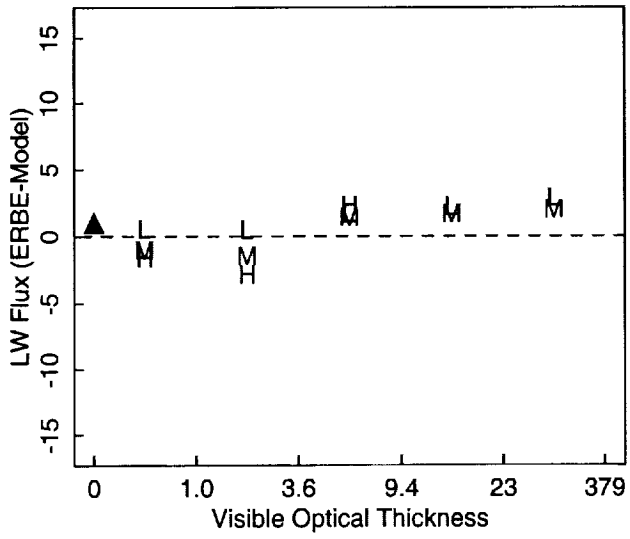
LW Flux (ERBE-Model)
15
10
5
0
-5
-10
-15
0
1.0
3.6
9.4
23
379
Visible Optical Thickness

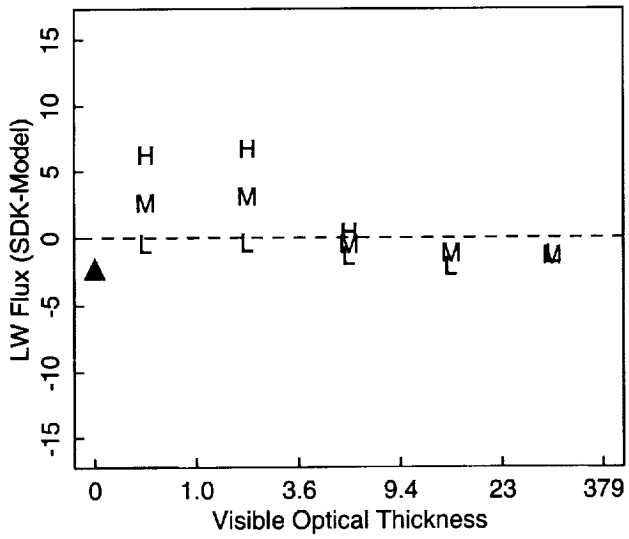
LW Flux (SDK-Model)
15
10
5
0
-5
-10
-15
0
1.0
3.6
9.4
23
379
Visible Optical Thickness

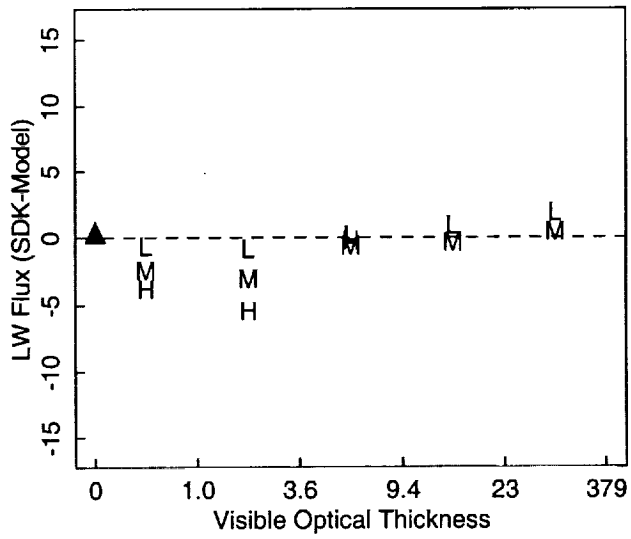
LW Flux (SDK-Model)
15
10
5
0
-5
-10
-15
0
1.0
3.6
9.4
23
379
Visible Optical Thickness

Fig. 9

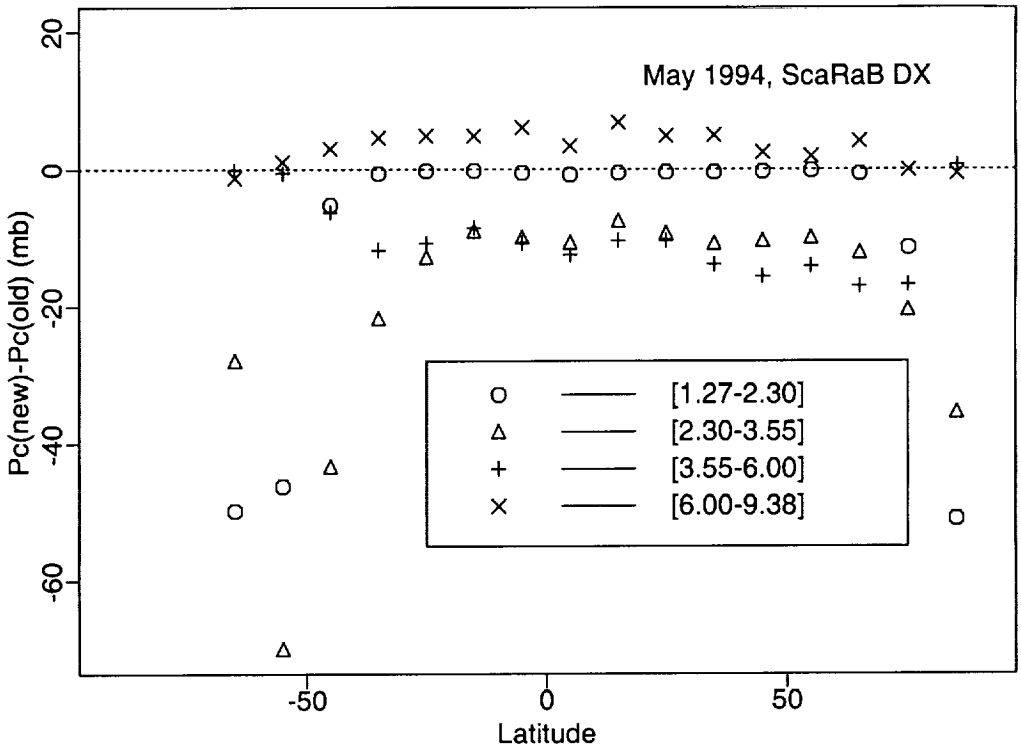
May 1994, ScaRaB DX
Pc(new)-Pc(old) (mb)
20
0
-20
-40
-60
-50
0
50
Latitude
[1.27-2.30]
[2.30-3.55]
[3.55-6.00]
[6.00-9.38]

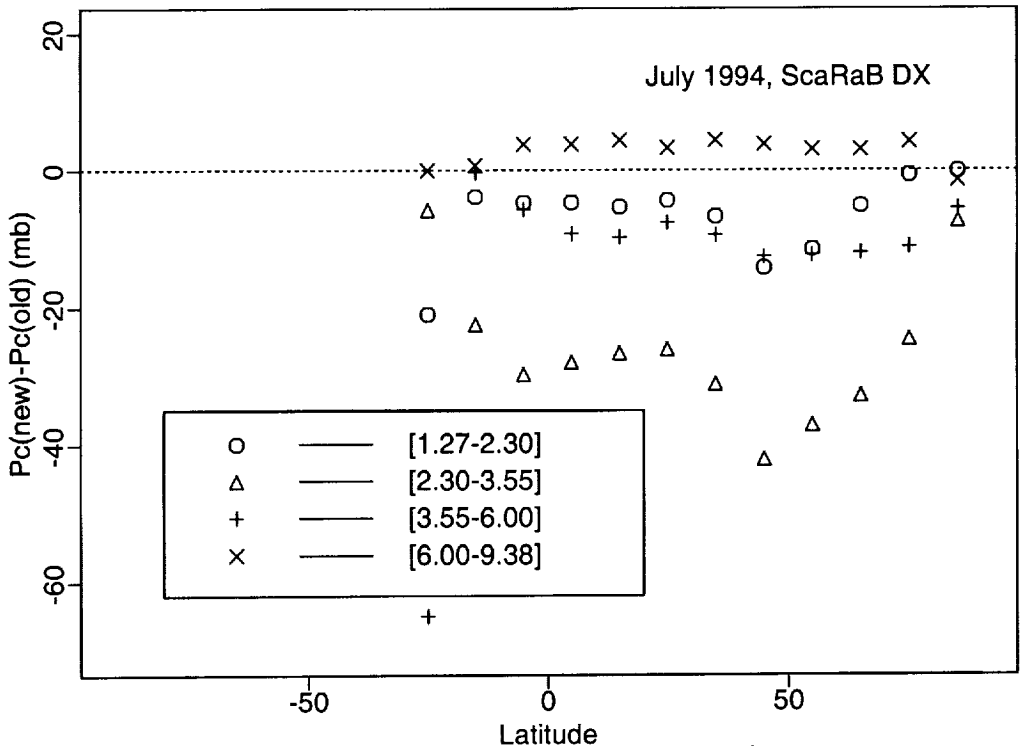
July 1994, ScaRaB DX
Pc(new)-Pc(old) (mb)
20
0
-20
-40
-60
-50
0
50
Latitude
[1.27-2.30]
[2.30-3.55]
[3.55-6.00]
[6.00-9.38]

Fig. A1

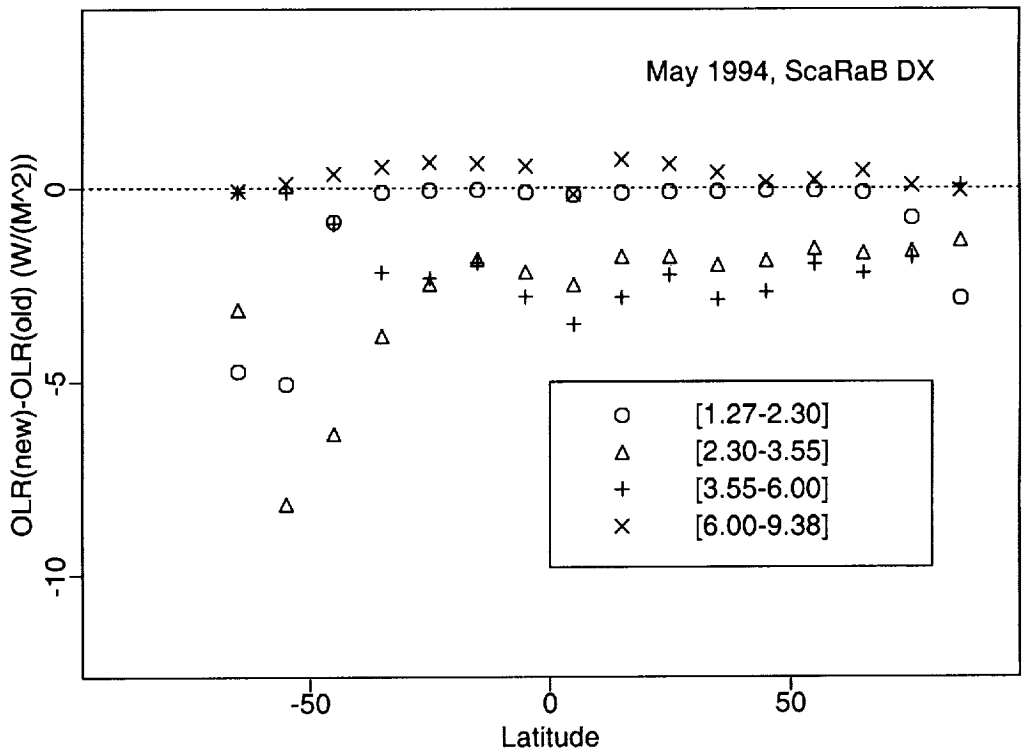
May 1994, ScaRaB DX
OLR(new)-OLR(old) (W/(M^2))
0
-5
-10
-50
0
50
Latitude
[1.27-2.30]
[2.30-3.55]
[3.55-6.00]
[6.00-9.38]

Fig. A2